



Probing the Origin of Changing-look Quasar Transitions with Chandra

Qian Yang¹, Paul J. Green¹, Chelsea L. MacLeod², Richard M. Plotkin^{3,4}, Scott F. Anderson⁵, Allyson Bieriyla¹,
Francesca Civano⁶, Michael Eracleous⁷, Matthew Graham⁸, John J. Ruan⁹, Jessie Runnoe¹⁰, and Xiurui Zhao¹

¹Center for Astrophysics | Harvard & Smithsonian, 60 Garden St., Cambridge, MA 02138, USA; qian.yang@cfa.harvard.edu

²BlackSky, 1505 Westlake Ave. N No. 600, Seattle, WA 98109, USA

³Physics Department, University of Nevada, Reno, 1664 N. Virginia St., Reno, NV 89557, USA

⁴Nevada Center for Astrophysics, University of Nevada, Las Vegas, NV 89154, USA

⁵Department of Astronomy, University of Washington, Box 351580, Seattle, WA 98195, USA

⁶NASA Goddard Space Flight Center, Greenbelt, MD 20771, USA

⁷Department of Astronomy & Astrophysics and Institute for Gravitation and the Cosmos, 525 Davey Laboratory, The Pennsylvania State University, University Park, PA 16802, USA

⁸Cahill Center for Astronomy and Astrophysics, California Institute of Technology, 1216 E. California Blvd., Pasadena, CA 91125, USA

⁹Department of Physics and Astronomy, Bishop's University, 2600 College St., Sherbrooke, QC J1M 1Z7, Canada

¹⁰Department of Physics and Astronomy, Vanderbilt University, Nashville, TN 37235, USA

Received 2023 April 23; revised 2023 June 14; accepted 2023 June 14; published 2023 August 2

Abstract

Extremely variable quasars can also show strong changes in broad-line emission strength and are known as changing-look quasars (CLQs). To study the CLQ transition mechanism, we present a pilot sample of CLQs with X-ray observations in both the bright and faint states. From a sample of quasars with bright-state archival SDSS spectra and (Chandra or XMM-Newton) X-ray data, we identified five new CLQs via optical spectroscopic follow-up and then obtained new target-of-opportunity X-ray observations with Chandra. No strong absorption is detected in either the bright- or the faint-state X-ray spectra. The intrinsic X-ray flux generally changes along with the optical variability, and the X-ray power-law slope becomes harder in the faint state. Large-amplitude mid-infrared variability is detected in all five CLQs, and it echoes the variability in the optical with a time lag expected from the light-crossing time of the dusty torus for CLQs with robust lag measurements. The changing-obscuration model is not consistent with the observed X-ray spectra and spectral energy distribution changes seen in these CLQs. It is highly likely that the observed changes are due to the changing accretion rate of the supermassive black hole, so the multiwavelength emission varies accordingly, with promising analogies to the accretion states of X-ray binaries.

Unified Astronomy Thesaurus concepts: [Accretion \(14\)](#); [Quasars \(1319\)](#); [Active galactic nuclei \(16\)](#); [Variable radiation sources \(1759\)](#); [Catalogs \(205\)](#)

1. Introduction

Active galactic nuclei (AGN) are powered by supermassive black holes (SMBHs) accreting gas, producing radiation that spans the entire electromagnetic spectrum (e.g., Elvis et al. 1994; Lusso et al. 2012). The X-ray emission comes from a hot corona (Haardt & Maraschi 1993) and possibly a jet (Narayan & Yi 1994; Blandford & Begelman 1999). In the UV/optical, there is continuum emission from the accretion disk (e.g., Shields 1978), as well as broad and narrow emission lines from the broad-line region (BLR) and narrow-line region (NLR), respectively (Davidson & Netzer 1979; Boroson & Green 1992). Dust in the torus is heated by the emission from the accretion disk and reemitted as thermal radiation in the infrared (Pier & Krolik 1993).

Observationally, AGN may be classified based on their multiwavelength characteristics. In the UV/optical, there are type 1 AGN with both broad ($\gtrsim 1000 \text{ km s}^{-1}$) and narrow ($\lesssim 1000 \text{ km s}^{-1}$) emission lines; there are also type 2 AGN with only narrow emission lines (Netzer 2015, and references therein). In the X-ray regime, there are unobscured AGN with $N_{\text{H}} < 10^{22} \text{ cm}^{-2}$ and obscured AGN with $N_{\text{H}} \geq 10^{22} \text{ cm}^{-2}$ (Ricci & Trakhtenbrot 2022, and references therein). Most type

1 AGN are X-ray unobscured, and most type 2 AGN are X-ray obscured (e.g., Koss et al. 2017; Ricci et al. 2017; Oh et al. 2022). The canonical AGN unified model interprets the different classes of AGN as the same class of object viewed at different angles (Antonucci 1993; Urry & Padovani 1995). In this model, AGN observed face-on, revealing unobscured emission from both the BLR and the NLR, are type 1. When viewed edge-on, the central and broad emission line (BEL) regions are obscured by the dusty torus, so we observe type 2 AGN with only narrow emission lines and high intrinsic columns of dust and gas.

However, there are some rare objects that suggest additional or complementary possibilities to this geometric model. Some type 2 AGN show no BELs but also no detectable obscuration even in X-rays (Panessa et al. 2009; LaMassa et al. 2014). Some of these “naked” type 2 AGN, selected for a lack of apparent BELs but AGN-like optical variability, do show faint BEL components in higher signal-to-noise ratio optical spectra (Barth et al. 2014; López-Navas et al. 2022).

Direct evidence that broad lines can strongly dim or even disappear in AGN, leaving only narrow lines, comes from “changing-look AGN” (CL AGN; e.g., Denney et al. 2014; Shappee et al. 2014; McElroy et al. 2016; Shapovalova et al. 2019; Trakhtenbrot et al. 2019). Remarkably, even the higher-luminosity quasars can change between different types on timescales of a year or less. Such objects exhibit large-amplitude changes in luminosity, accompanied by the dramatic

emergence or near disappearance of BEL components, dubbed “changing-look quasars” (CLQs; e.g., LaMassa et al. 2015; MacLeod et al. 2016; Ruan et al. 2016; Runnoe et al. 2016; Gezari et al. 2017; Yang et al. 2018). The changing-look phenomena were also found in $z > 2$ quasars with dramatic changes in their C IV emission lines (Ross et al. 2020). Repeat spectroscopy for large quasar samples continues to uncover this rare and remarkable phenomenon in regimes of luminosity and redshift that now overlap the large cosmological samples of quasars of the Sloan Digital Sky Survey (SDSS; Schneider et al. 2010; Lyke et al. 2020; Green et al. 2022; Almeida et al. 2023).

The discovery of CLQs profoundly affects many areas of astrophysics, including our understanding of quasar duty cycles (e.g., Martini & Schneider 2003) and galaxy evolution (Kormendy & Ho 2013), through distinct feedback processes in states of high and low accretion rate (e.g., Fabian 2012). Rapid swings in the SMBH accretion rate may also explain the complex AGN/star formation connection (e.g., Hickox et al. 2014) and help reconcile cosmological simulations with the observed prevalence of an ionized intergalactic medium or “AGN proximity zone fossils” (Oppenheimer et al. 2018). These intriguing prospects explain why CLQs have been ardently sought in the last few years, resulting in at least 80 now known (e.g., LaMassa et al. 2015; MacLeod et al. 2016; Ruan et al. 2016; Yang et al. 2018; Frederick et al. 2019; MacLeod et al. 2019; Sheng et al. 2020; Hon et al. 2022; Green et al. 2022; Zeltyn et al. 2022).

Several explanations for the strong and relatively rapid luminosity and BEL changes have been proposed. The first direct explanation is the changing obscuration due to moving clouds crossing over our line of sight. The term “changing-look” was originally used to describe objects whose X-ray spectra showed the absorption changing between Compton thick and Compton thin. Absorption changes are a widely accepted explanation for X-ray changing-look events (e.g., Matt et al. 2003; Bianchi et al. 2005; Piconcelli et al. 2007; Ballo et al. 2008; Marchese et al. 2012; Ricci et al. 2016). Clouds in the BLR or torus may plausibly eclipse the much smaller X-ray emission region (Maiolino et al. 2010). However, the crossing time for intervening clouds orbiting outside the BLR is too long (LaMassa et al. 2015) compared to observed CLQ transition timescales. A tidal disruption event (TDE), in which a star is disrupted by and accretes onto an SMBH, is also a mechanism for strong, rapid variability. However, TDEs can only explain a few turn-on CLQ cases (e.g., Eracleous et al. 1995; Merloni et al. 2015; Blanchard et al. 2017), and TDE flares are inconsistent with most CLQ light-curve shapes and bright-state durations (MacLeod et al. 2016; Yang et al. 2018; Green et al. 2022). A nuclear supernova (SN) explosion could also cause a luminous nuclear flare, but the timescale and mid-infrared (MIR) color variability of SNe are inconsistent with CLQs (Yang et al. 2019). Large accretion rate changes seem the most likely explanation, as suggested by recent work (LaMassa et al. 2015; Runnoe et al. 2016; Yang et al. 2018; MacLeod et al. 2019; Green et al. 2022). However, for major accretion rate changes, the radial inflow timescales ($\sim 10^4$ yr; Krolik 1999) are inconsistent with the observed transition timescale of CLQs, from a few months to decades (e.g., Yang et al. 2018; this work). A combination of factors may be necessary to explain some CLQ behavior; e.g., rapid changes in the UV ionizing continuum mediate both the illumination of

the BLR and the sublimation or re-formation of dust in the inner torus, just outside the BLR (Zeltyn et al. 2022).

Strong accretion state transitions are also seen in X-ray observations of the Galactic X-ray binaries (XRBs; e.g., Maccarone 2003; Debnath et al. 2010; Kara et al. 2019; Wang et al. 2022), suggesting analogies between AGN and XRB accretion (e.g., Ruan et al. 2019; Jin et al. 2021). While typical black hole (BH) accretion regions cannot yet be spatially resolved, temporal changes in XRB spectral states have gone a long way toward uncovering the accretion physics in XRBs and suggest powerful theoretical and observational analogies to AGN and quasars (Narayan 2005; Merloni et al. 2003; McHardy 2010; Ruan et al. 2019). However, mass scaling from XRBs to SMBHs (e.g., Sobolewska et al. 2011; Schawinski et al. 2010) suggests timescales ($\sim 10^{4-7}$ yr) for quasar accretion state transitions. Clearly, CLQ transition timescales do not scale as expected from XRBs (Stern et al. 2018). Thus, large spectral state changes in quasars challenge and invigorate debates about both accretion theory and the nature of historical quasar classes (i.e., type 1 versus type 2; Elitzur et al. 2014). Some recent studies suggest that the timescale problem can be qualitatively alleviated when taking the large-scale magnetic field into account (Dexter & Begelman 2019; Pan et al. 2021) or considering accretion disk instabilities (e.g., the radiation pressure instability; Sniegowska et al. 2020).

Comparison of multiwavelength observations before and after a transition is needed to test different models of CLQs. With X-ray spectra in both states, we can detect changes in obscuration or X-ray spectral power-law slopes. The X-ray spectral shape variations were observed in a handful of CL AGN at lower luminosities (Seyfert galaxies), including Mrk 1018 (Husemann et al. 2016), Mrk 590 (Denney et al. 2014), NGC 1566 (Parker et al. 2019), and 1ES 1927+65 (Trakhtenbrot et al. 2019). Hardening of the X-ray-to-UV spectrum of the fading CL AGN Mrk 1018 suggests accretion state transitions similar to XRBs (Noda & Done 2018). Object Mrk 1018 also shows evidence that both the X-ray photon index and α_{OX} , similar to some XRBs, exhibit V-shaped correlations (negative/positive correlation below/above a critical value) in a single AGN (Lyu et al. 2021). In comparison to quasars, however, these AGN tend to have ~ 10 – 100 times lower SMBH masses, high Eddington ratios, and unusual, X-ray-bright spectral energy distributions (SEDs).

The first CLQ, SDSS J015957.64+003310.5 (hereafter J0159), discovered by LaMassa et al. (2015) is an X-ray-selected AGN, and there are serendipitous X-ray observations: an XMM-Newton observation in its bright state and a Chandra observation in its faint state. LaMassa et al. (2015) analyzed its X-ray spectra and found that its X-ray flux dropped by a factor of 7 with no change in absorption. Ai et al. (2020) analyzed the X-ray data of a CLQ, SDSS J155258+273728 (hereafter J1552), discovered by Yang et al. (2018) and found that the absorption in X-rays is moderate and stable, and the X-ray spectrum becomes harder in the bright state, with the Eddington ratio being lower than a few percent in both states. They found that the CL AGN and CLQ with X-ray observations in both states follow a V-shaped correlation; above a critical turnover luminosity, the X-ray spectrum is softer when brighter, and below the critical luminosity, the trend is reversed as harder when brighter. Ruan et al. (2019) obtained Chandra X-ray observations of five CLQs and found

Table 1
Changing-look Quasars

Full Name	Short Name	R.A.	Decl.	Redshift
SDSS J020621.67–060952.7	J0206	02:06:21.67	–06:09:52.70	0.413
SDSS J022429.10–091851.7	J0224	02:24:29.10	–09:18:51.70	0.357
SDSS J082905.98+420204.3	J0829	08:29:05.98	+42:02:04.30	0.638
SDSS J122638.66–001114.0	J1226	12:26:38.66	–00:11:14.06	0.642
SDSS J133806.59–012412.8	J1338	13:38:06.59	–01:24:12.84	0.452

consistency with the accretion state transitions in prototypical XRB outbursts, as well as a possible V-shaped correlation for the UV–to–X-ray spectral index with an inversion correlation at a critical Eddington ratio of $\sim 10^{-2}$. However, for those five CLQs, only ROSAT All-Sky Survey measurements are available for the bright state, yielding upper limits on the bright-state X-ray luminosity (and thus lower limits on α_{OX}). Jin et al. (2021) performed Chandra observations for 10 CLQs and further investigated the similarities between AGN and XRBs. However, among those 10 CLQs, only two (J2252 and J2333) had archival XMM-Newton X-ray detections in their former bright states; there are again only upper limits on the bright-state X-ray luminosity (and thus lower limits on α_{OX}) for the remaining eight CLQs, preventing much analysis of the changes in obscuration or X-ray spectral power-law slopes for CLQs.

To test the different models of CLQs and probe the structure of AGN and the accretion processes of SMBHs, we pursue a study of CLQs with X-ray observations in both states. In this work, we present a pilot sample of five new CLQs with X-ray observations in both states. Our sample doubles the number of optical spectroscopic confirmed CLQs. Here, for clarity, CLQs are CL AGN with $L_{\text{bol}} \gtrsim 10^{45}$ erg s $^{-1}$ in the bright state with X-ray observations in both states. The five new CLQs are SDSS J020621.67–060952.7 (hereafter J0206) at $z = 0.413$, SDSS J022429.10–091851.7 (hereafter J0224) at $z = 0.357$, SDSS J082905.98+420204.3 (hereafter J0829) at $z = 0.638$, SDSS J122638.66–001114.0 (hereafter J1226) at $z = 0.642$, and SDSS J133806.59–012412.8 (hereafter J1338) at $z = 0.452$. All of these quasars have been observed to dim due to our selection criteria, as described below.

This paper is organized as follows. We present the target selection, data, and reduction in Section 2. In Section 3, we describe the data analysis methods, including optical spectral fitting, X-ray spectral analysis, and SED fitting. Results and discussions are in Sections 4 and 5, respectively. We summarize the paper in Section 6. Throughout this paper, we adopt a standard Λ CDM cosmology with $\Omega_{\Lambda} = 0.7$, $\Omega_m = 0.3$, and $H_0 = 70$ km s $^{-1}$ Mpc $^{-1}$.

2. Selection, Data, and Reduction

2.1. CLQ Target Selection

We selected candidates from the SDSS quasar catalogs (Schneider et al. 2010; Pâris et al. 2018), applying a redshift limit of $z < 0.9$ to keep H β within the SDSS spectral range. Radio-detected objects were excluded using the FIRST survey (Becker et al. 1995, with a detection limit of 1 mJy), since jet-dominated emission in the bright state and its variability would complicate our interpretations. To study CLQs in both states, we required existing archival XMM-Newton or Chandra observations close in time to the SDSS spectroscopic observations. For these X-ray-observed quasars, we compiled

optical light curves from multiple imaging surveys (see Section 2.2) and selected CLQ candidates with a large-amplitude optical variability, specifically $|\Delta g| > 1$ and $|\Delta r| > 0.5$ mag (as described in MacLeod et al. 2019), comparing the latest available epoch (at the time before optical spectroscopic follow-up) to the bright state.

We obtained new optical follow-up spectra using 6–8 m telescopes (Section 2.3) as the CLQ candidates dramatically faded in the optical. Once we confirmed with a follow-up optical spectrum a 3σ fading of the broad H β flux, we triggered a Chandra X-ray target-of-opportunity (ToO) observation (Section 2.4), as well as radio observations with the Karl G. Jansky Very Large Array (VLA; Section 2.5). We summarize the basic properties of the five observed CLQs in Table 1.

2.2. Optical Imaging Data

We used multiple publicly available optical imaging surveys, including the SDSS imaging survey in the *ugriz* bands (Abazajian et al. 2009), Pan-STARRS1 (PS1) in the *grizy* bands (Chambers et al. 2016), the Palomar Transient Factory (PTF) survey in the *g* and *R* bands (Law et al. 2009), and the Zwicky Transient Facility (ZTF) survey in the *gri* bands (Bellm et al. 2019). We compiled *g*- and *r*-band light curves from these surveys using the point-spread function (PSF) magnitudes. For objects without recent public ZTF photometric data, we performed imaging observations in the *g* and *r* bands using the 1.2 m telescope at the Fred Lawrence Whipple Observatory (FLWO) on Mount Hopkins in Arizona.

To calibrate the optical data from different surveys onto the same flux scale for light-curve plotting, we applied corrections to account for different filter curves. We convolved each quasar spectrum with the PS1, PTF, ZTF, and FLWO filter curves to obtain synthetic magnitudes and derived the magnitude offsets, typically ~ 0.02 mag in the *g* band and 0.09 mag in the *r* band, between similar filters from different surveys. We used these offsets to calibrate all optical magnitudes to SDSS filter system magnitudes for the purposes of light-curve plotting.

We also used the Catalina Real-time Transient Survey (CRTS; Drake et al. 2009). The CRTS photometric data are unfiltered, so we applied a constant offset to match the contemporaneous *r*-band light curve described above. We describe the photometric data we used for SEDs in Section 3.3 and summarize the photometric data in Table B1.

We corrected the Galactic extinction using the dust reddening map of Schlegel et al. (1998, SFD) and the reddening law in Fitzpatrick (1999). The typical $E(B - V)_{\text{SFD}}$ for the five CLQs is 0.02 mag. We computed the extinction coefficients for the surveys we used in this work (see more details in Appendix A). We adopt $R_V = 3.1$, employing the traditional value of R_V in the diffuse interstellar medium (Cardelli et al. 1989).

Table 2
Spectroscopic Observations

Name	MJD	Date	Telescope	Spectrograph	Grating lines mm ⁻¹	ExpTime s	State
J0206	56,660	2014-01-03	SDSS	Bright
J0206	58,431	2018-11-09	MMT	Binospec	270	2000	Faint
J0206	58,507	2019-01-24	Gemini	GMOS-N	400	3000	Faint2
J0224	51,908	2000-12-30	SDSS	Bright
J0224	59,145	2020-10-23	MMT	Binospec	270	1800	Faint
J0829	55,513	2010-11-13	SDSS	Bright
J0829	58,866	2020-01-18	MMT	Binospec	270	2700	Faint
J0829	58,968	2020-04-29	HET	LRS2-R	Red 920 (far red 800)	3000	Faint2
J1226	51,990	2001-03-22	SDSS	Bright
J1226	54,153	2007-02-22	SDSS	Intermediate
J1226	58,574	2019-04-01	MMT	Binospec	270	3200	Faint
J1338	52,427	2002-06-02	SDSS	Bright
J1338	57,818	2017-03-06	MMT	Blue Channel	300	1800	Faint
J1338	57,891	2017-05-18	APO 3.5 m	DIS	Blue 400 (red 300)	900	Intermediate
J1338	58,162	2018-02-13	Magellan	IMACS	300	1800	Intermediate2

Note. Date is in the format of year-month-day. ExpTime stands for “exposure time.”

2.3. Optical Spectroscopic Observations

For the bright state, we use the SDSS spectra taken by the Sloan Foundation 2.5 m telescope (Gunn et al. 2006) at Apache Point Observatory (APO). The spectra are from the SDSS-I/II, obtained between 2000 and 2014 with a wavelength coverage of 3800–9100 Å, and the Baryon Oscillation Spectroscopic Survey (Dawson et al. 2013) spectrograph of the SDSS-III (Eisenstein et al. 2011), with a wider wavelength coverage of 3600–10400 Å (Smee et al. 2013). The SDSS spectral resolution is 1500 at 3800 Å and 2500 at 9000 Å.

We obtained optical spectroscopic follow-up for CLQ candidates in the faint states from 2017 to 2020. Table 2 summarizes the spectroscopic observation information, including telescope, grating, and exposure time.

The MMT telescope is a 6.5 m telescope on Mount Hopkins in Arizona. Object J1338 was observed with the Blue Channel spectrograph using a grating of 300 lines mm⁻¹ with a resolution of 6.47 Å and wavelength coverage of 5268 Å. For the other four targets, we used the Binospec spectrograph with a grating of 270 lines mm⁻¹ with a resolution of 1340 and wavelength coverage of 3900–9240 Å.

The Gemini Observatory consists of twin 8.1 m diameter telescopes, Gemini North and Gemini South, which are located at two separate sites on Maunakea in Hawaii and Cerro Pachón in Chile, respectively. We obtained Gemini North observations for J0206 to cover the H β and H α emission lines simultaneously. We used the Gemini Multi-Object Spectrograph (GMOS-N) with the R400 grating (400 lines mm⁻¹) with a resolution of 1918 and wavelength coverage of 4160 Å.

The 3.5 m telescope at APO is located in the Sacramento Mountains in Sunspot, New Mexico. We used the Double Imaging Spectrometer (DIS), which is a medium-dispersion spectrograph with separate red and blue channels. In the blue (red) channel, we used the B400 (R300) grating of 400 (300) lines mm⁻¹ with a wavelength coverage of 3660 (4620) Å. Soon after our initial follow-up, MMT observations confirmed J1338 to be a CLQ in the faint state; it rebrightened, as

confirmed using the APO 3.5 m telescope after our Chandra observations.

The Hobby–Eberly Telescope (HET) is a 10 m aperture telescope located at the McDonald Observatory in the Davis Mountains in Texas. We used the LRS2-R spectrograph, which simultaneously covers 6450–8400 Å (red arm) and 8275–10500 Å (far red arm) at a resolving power of 1800 in each channel, respectively (Chonis et al. 2016).

The Magellan Telescopes are a pair of 6.5 m telescopes located at Las Campanas Observatory in Chile. We used the Inamori Magellan Areal Camera and Spectrograph (IMACS) on the Baade telescope with a grating of 300 lines mm⁻¹ with wavelength coverage of 3650–9740 Å. We used the Magellan Baade telescope to observe J1338 a few months after the Chandra observations.

The spectra were reduced using standard IRAF¹¹ routines (Tody 1986, 1993). Since the absolute flux calibrations from the follow-up spectra were not always reliable, we normalized the spectra to the earlier SDSS spectrum assuming a constant narrow emission line luminosity (described in Section 3.1).

All of the spectra of the five CLQs are shown in Figure 1. The spectra in black are the earliest SDSS spectra in the bright state. The spectra in red are our follow-ups in the faint state. For some of them, there are intermediate spectra (green and orange) observed by SDSS or our follow-ups.

2.4. X-Ray Observations

We used archival X-ray observations close in time to the optical spectra from the Chandra Source Catalog (Evans et al. 2020) or the XMM-Newton serendipitous survey (4XMM-DR10; Traulsen et al. 2020). For X-ray-observed CLQ candidates confirmed as CLQs by optical follow-up spectra, we obtained Chandra ToO observations. Our Chandra observations were triggered shortly after our optical spectroscopic follow-ups. The targets were observed using the

¹¹ IRAF is distributed by the National Optical Astronomy Observatory, which is operated by the Association of Universities for Research in Astronomy (AURA) under cooperative agreement with the National Science Foundation.

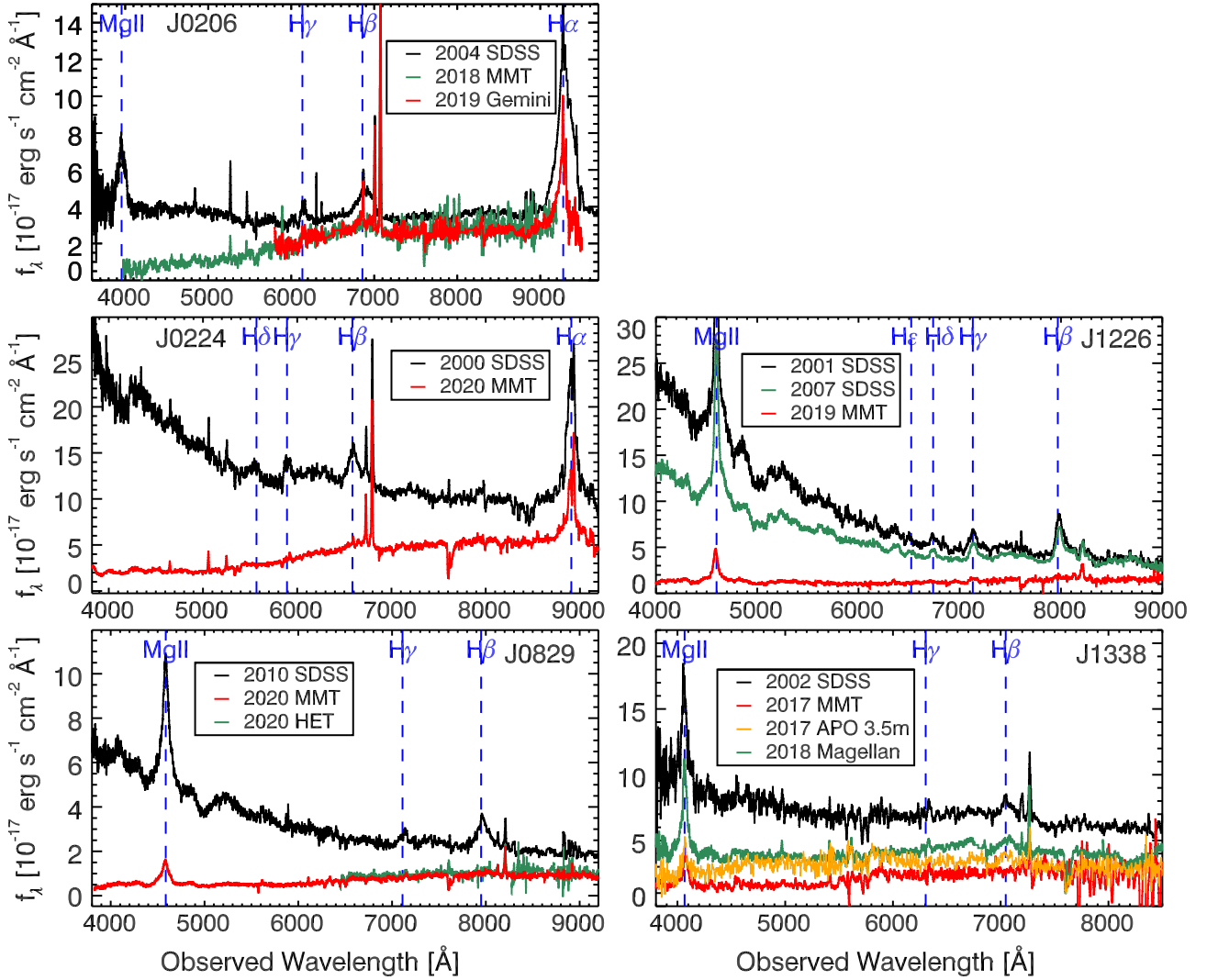


Figure 1. Optical spectra for five new CLQs, including J0206 (top left), J0224 (middle left), J0829 (bottom left), J1226 (middle right), and J1338 (bottom right). The y-axis is the flux density, f_λ , in units of $10^{-17} \text{ erg s}^{-1} \text{ cm}^{-2} \text{ \AA}^{-1}$. The black spectra are from SDSS in bright states. The red spectra are our spectroscopic follow-ups in faint states. For some CLQs, there are spectra in intermediate states (green and orange). The vertical blue dashed lines mark the expected central wavelengths of BELs. The spectra in the faint states obviously show that the continuum emission faded dramatically, accompanied by the disappearance of BELs.

Advanced CCD Imaging Spectrometer detector (Garmire et al. 2003). The X-ray observations are listed in Table 3.

Four of the CLQ candidates were observed in X-rays in both the bright and faint states. However, J1338 is a special case. In 2017 March (MJD 57,818), we obtained an optical spectrum of the XMM-Newton source and CLQ candidate J1338, for which analysis showed that the broad $H\beta$ line had vanished at $\geq 3\sigma$ significance with respect to the earlier SDSS spectrum. Shortly afterward, we began monitoring the source with the 1.2 m telescope at FLWO, which confirmed the object to be in the faint state according to the g -band magnitude. We triggered the Chandra observation in mid-April, but it was observed by Chandra about 3 weeks later, during which we saw an unexpected ~ 1 mag brightening in the g band. The resulting Chandra spectrum showed a bright, unobscured, normal AGN power-law slope, as expected after its rebrightening. Just after the Chandra observation, we obtained an optical spectrum with the 3.5 m telescope at APO in June that showed significant broad $H\beta$ emission line flux (spectrum plotted in orange in Figure 1). The light curve of J1338 indicates a transition from

the faint to the bright state of about 40 days, which is very rapid, even for a CLQ.

For the Chandra data reduction, we used CIAO version 4.14 (Fruscione et al. 2006) and CALDB version 4.9.6. We used the `chandra_repro` reprocessing script, which automates the recommended data processing steps in CIAO.

For the archival XMM-Newton data reduction, we used the Science Analysis Software (Gabriel et al. 2004) version 20.0.0 following standard procedures. The XMM-Newton data are from three X-ray CCD cameras, including two MOS cameras (MOS1 and MOS2) and one pn camera.

2.5. Radio Observations

If the CLQ dim states represent a radiatively inefficient accretion (RIAF) state, they should reactivate a compact radio jet, as seen in low-luminosity AGN (Ho 2008). We triggered radio observations using the VLA for four of the five CLQs, omitting J1338 because it had returned rapidly to the bright state. The VLA consists of 27 independent antennas, each of which has a dish diameter of 25 m (Thompson et al. 1980;

Table 3
X-Ray Observations

Name	Telescope	ObsID	PI	MJD	Date	Exposure ks	Net Counts	Group	Epoch
J0206	XMM	677670138	Pierre	55,945	2012-01-19	10.7	20.23/18.22/18.22	1	
J0206	XMM	677670139	Pierre	55,945	2012-01-19	14.3	24.63/29.77/18.83	1	
J0206	XMM	747190632	Pierre	56,691	2014-02-03	24.3	170.54/157.70/300.24	2	
J0206	XMM	742430201	Mantz	56,837	2014-06-29	30.8	640.84, 623.45, 436.19	3	1
J0206	Chandra	16575	Mantz	57,197	2015-06-24	4.991	36.88	4	
J0206	Chandra	20457	Green	58,483	2018-12-31	19.84	345.86	5	2
J0206	Chandra	22027	Green	58,483	2018-12-31	19.84	315.39	5	2
J0224	XMM	655343850	Finoguenov	55,582	2011-01-21	2.7	48.72, 58.51, 219.87	1	1
J0224	Chandra	23662	Green	59,279	2021-03-06	24.95	357.87	2	2
J0224	Chandra	24978	Green	59,280	2021-03-07	23.96	389.57	2	2
J0829	XMM	724791301	Dennerl	56,573	2013-10-08	26.2	128.53, 149.15, 175.94	1	1
J0829	XMM	724791332	Dennerl	56,574	2013-10-09	8.7	89.97, 89.88, 115.24	1	1
J0829	XMM	724791333	Dennerl	56,574	2013-10-09	8.7	46.86, 44.57, 46.28	1	1
J0829	Chandra	22550	Green	58,967	2020-04-28	17.72	77.17	2	2
J0829	Chandra	23234	Green	58,972	2020-05-03	29.4	124.99	2	2
J1226	Chandra	4865	Richards	53,047	2004-02-12	4.899	145.68	1	1
J1226	Chandra	21412	Green	58,606	2019-05-03	16.84	141.47	2	2
J1226	Chandra	22204	Green	58,607	2019-05-04	17.83	134.38	2	2
J1226	Chandra	22205	Green	58,608	2019-05-05	11.91	86.96	2	2
J1338	XMM	502060101	Lamastra	54,292	2007-07-11	17.6	68.44, 87.38, 224.18	1	1
J1338	Chandra	19474	Green	57,881	2017-05-08	32.64	924.96	2	2

Note. ObsID stands for “observation ID.” Net counts for XMM-Newton (XMM) are for the MOS1, MOS2, and pn cameras, respectively.

Table 4
Radio Observations

Name	Project	Config.	Phase Cal.	MJD	Date	Robust	f_{peak} $\mu\text{Jy beam}^{-1}$	$\log L_5$ GHz erg s $^{-1}$	$\log(R)$
J0206	18B-393	C	J0239–0234	58,483	2018-12-31	0.0	47.1 ± 5.4	39.01	–4.79
J0224	SM0081	A	J0239–0234	59,279	2021-03-06	0.0	50.1 ± 4.5	38.90	–5.03
J0829	SL0102	C	J0818+4222	58,968	2020-04-29	1.0	13.8 ± 2.8	38.86	–5.25
J1226	SK0063	B	J1224+0330	58,609	2019-05-06	0.5	28.4 ± 5.2	39.18	–5.15

Note. Here f_{peak} is reported at 6.2 GHz for J0206, J0224, and J1226 and 6.0 GHz for J0829; R is the radio-loudness, $R = L_5 \text{ GHz}/L_{2500 \text{ \AA}}$.

Perley et al. 2011). The VLA observations were performed within 1 day of the Chandra X-ray observations.

Each VLA observation lasted 2 hr, except for J1226, which lasted 1 hr. This yielded 87 minutes on source (38 minutes for J1226). Observations were taken in the C band with 2×2 GHz basebands centered at 5.25 and 7.2 GHz for the near-equatorial sources J0206, J0224, and J1226 (to minimize interference from satellites within the Clarke Belt) and 5.0 and 7.0 GHz for J0829. We set the flux density scale and performed bandpass calibrations using 3C 147 (for J0206 and J0224) or 3C 286 (for J0829 and J1226), and we cycled to a nearby phase calibrator to solve for the complex gain solutions (see Table 4 for the phase calibrator and array configuration used for each observation).

The VLA data were processed using the Common Astronomy Software Applications (CASA) v6.1.2.7 (CASA Team et al. 2022) and calibrated using the VLA calibration pipeline 6.1.2, following standard procedures. The data were imaged using `tclean`, adopting two Taylor terms to model the spectral dependence of sources in the field and Briggs weighting with a `robust` value for each source as noted in Table 4. We detected radio emission at the known optical

position of each target, and flux densities were measured using `imfit` by fitting a two-dimensional Gaussian to each source. We found that J0224 and J1226 are consistent with point sources, and J0206 and J0829 are extended ($3.0'' \times 0.5''$ and $6.8'' \times 4.5''$, respectively, after deconvolution with the synthesized beam). The signal-to-noise ratio of the radio detections is not large enough to obtain meaningful in-band constraints on the radio spectral indices of our targets. We summarize the radio observations in Table 4.

2.6. Infrared Data

The Wide-field Infrared Survey Explorer (WISE; Wright et al. 2010) mapped the sky in 2010 in four bands centered at MIR wavelengths of 3.4, 4.6, 12, and 22 μm (W1, W2, W3, and W4). WISE scans the sky every half-year in the W1 and W2 bands. We used unWISE (Lang 2014; Meisner et al. 2023) light curves force-photometered for sources in the DESI Legacy Imaging Surveys (Dey et al. 2019).

We also compiled the available near-infrared (NIR) data, including the UKIRT Infrared Deep Sky Survey (UKIDSS;

Lawrence et al. 2007) in the *YJHK* bands, the UKIRT Hemisphere Survey (UHS; Dye et al. 2018) in the *J* band, and the VISTA Hemisphere Survey (VHS; McMahon et al. 2013) in the *YJHK_s* bands.

3. Data Analysis

3.1. Optical Spectral Fitting

We fit the optical spectra following the quasar spectral fitting code `QSOFIT` (Shen et al. 2019). The spectra are fit in the rest frame of the quasar after correcting for Galactic reddening, again using the dust map of Schlegel et al. (1998) and the extinction curve from Cardelli et al. (1989).

The `QSOFIT` code decomposes different components in the quasar spectrum, including power-law continuum, Fe II emission multiplets, and major broad and narrow emission lines. It uses empirical UV Fe II emission templates from the literature (Vestergaard & Wilkes 2001; Tsuzuki et al. 2006; Salvander et al. 2007) covering 1000–3500 Å and an optical Fe II template (3686–7484 Å) from Boroson & Green (1992).

The `QSOFIT` code is designed for quasar spectral fitting, where the host galaxy emission is not prominent, so no host galaxy components were included initially. For our CLQs in the faint states when the AGN continuum is dim, the host galaxy emission becomes more obvious. Therefore, we enhanced the code to take into account host galaxy stellar emission using simple stellar population models (Bruzual & Charlot 2003) with the Chabrier (2003) initial mass function. We allow for two host components, one for the young (<300 Myr) stellar population and one for old (>300 Myr) stellar populations. We use 30 templates from Bruzual & Charlot (2003) covering metallicities of $Z = 0.004, 0.02, \text{ and } 0.05$ and the ages of young (0.005, 0.025, 0.10, and 0.29 Gyr) and old (0.64, 0.90, 1.4, 2.5, 5, and 11 Gyr) populations.

Following Shen et al. (2019), we choose a few continuum windows and fit the continuum components described above together. The emission lines are fit after subtracting the fitted continuum model. Three broad and one narrow Gaussian component are used for the $H\beta$ and $H\alpha$ emission.

According to the empirical $L_{[\text{O III}]} - R_{\text{NLR}}$ relation of Bennert et al. (2002), the size of the [O III] narrow emission line region for our CLQs is at most 2–3 kpc, corresponding to $\sim 10^4$ lt-yr, so the narrow-line flux is certainly expected to remain constant on decadal timescales. The SDSS fiber sizes are 2''–3'', and our follow-up spectral slit widths are 1''. At the redshifts of our CLQ sample, the scale is 7.7 kpc arcsec⁻¹, so the NLRs are fully encompassed by the spectral apertures, even accounting for seeing. We use the first SDSS epoch as the reference spectrum and rescale the other spectra to the first SDSS epoch according to the flux of the narrow [O III] and then fit the spectra as described above.

To quantify the measurement uncertainties, we used a Monte Carlo approach by adding a random Gaussian deviate to the flux at each pixel, with the Gaussian σ equal to the spectral error at that pixel. We compute the values and their uncertainties using the median value and the semiamplitude of the range enclosing the 16th and 84th percentiles of the distribution from 100 trials.

Figure 2 shows an example of the optical spectral fitting to J0224 in the bright (left panels) and faint (right panels) states. The top panels show the continuum decomposition. In the bright state, the continuum is dominated by the AGN power-

law continuum. Weak stellar emission from the host is also detected. In the faint state, the AGN continuum emission dims dramatically; thus, the continuum becomes dominated by the host stellar emission. The middle two panels show the spectral fitting in the $H\beta$ window. There is obvious broad $H\beta$ emission in the bright state, but it becomes invisible in the faint state. The bottom two panels are in the $H\alpha$ window. The broad $H\alpha$ emission becomes much weaker but remains visible in the faint state.

To evaluate the variability of broad $H\beta$ emission, we calculate the flux deviation between the bright- and faint-state spectra in the $H\beta$ window (4750–4940 Å) following MacLeod et al. (2019) and Green et al. (2022) as

$$N_\sigma(\lambda) = (f_{\text{bright}} - f_{\text{faint}}) / \sqrt{\sigma_{\text{bright}}^2 + \sigma_{\text{faint}}^2}, \quad (1)$$

where f is the flux density in units of $\text{erg s}^{-1} \text{cm}^{-2} \text{\AA}^{-1}$, and σ is its uncertainty. Following the procedures in MacLeod et al. (2019) and Green et al. (2022), we subtract the continuum model, rebin the spectrum to 2\AA pixel^{-1} in the rest frame, and smooth the spectrum with a window of 32\AA .¹²

We characterize the significance of the $H\beta$ change as the maximum flux deviation of the line relative to the continuum at 4750 Å as follows:

$$N_\sigma(H\beta) = N_\sigma(4750 - 4940 \text{\AA}) - N_\sigma(4750 \text{\AA}). \quad (2)$$

To estimate the BH mass, M_{BH} , for each of our CLQs, we utilize the single-epoch virial BH mass method using the bright-state spectrum with its prominent BELs. In this approach, the M_{BH} is estimated using the measured width of a broad Balmer emission line, as well as an empirical radius–luminosity relation for the BLR based on reverberation mapping results of low-redshift AGN. We use the relation (Equation (6)) in Vestergaard & Peterson (2006) as follows:

$$M_{\text{BH}} = 10^{6.91 \pm 0.02} \left[\frac{\text{FWHM}(H\beta)}{1000 \text{ km s}^{-1}} \right]^2 \times \left[\frac{L(H\beta)}{10^{42} \text{ erg s}^{-1}} \right]^{0.5} M_\odot, \quad (3)$$

where $\text{FWHM}(H\beta)$ and $L(H\beta)$ are the FWHM (i.e., the width) and luminosity of the broad $H\beta$ emission. We calculate the Eddington luminosity using $L_{\text{Edd}} = 1.26 \times 10^{38} M_{\text{BH}}$ in units of erg s^{-1} .

3.2. X-Ray Spectral Analysis

For X-ray spectral analysis and fitting, we used the `XSPEC` software (Arnaud 1996) in version 12.12.0. We grouped X-ray spectra observed with the same telescope within 1 week and performed spectral analysis together, indicated by the column “Group” in Table 3. In `XSPEC`, the spectra are rebinned using the task `grppha` so that each spectral bin contains 20, 15, 10, 5, 3, or 1 count, with total net counts, N_{net} , of $N_{\text{net}} \geq 300$, $225 \leq N_{\text{net}} < 300$, $100 \leq N_{\text{net}} < 225$, $50 \leq N_{\text{net}} < 100$, $30 \leq N_{\text{net}} < 50$, and $10 \leq N_{\text{net}} < 30$, respectively. We used χ^2 statistic for high-count spectra and a C statistic (Cash 1979) when the counts in each spectral bin are less than 20.

The intrinsic AGN X-ray spectrum is typically a power law within the Chandra and XMM-Newton energy range. The

¹² We also tested a smaller spectral smoothing window of 16 Å, and the calculated $N_\sigma(H\beta)$ values are slightly larger ($\sim 10\%$) than those using 32 Å.

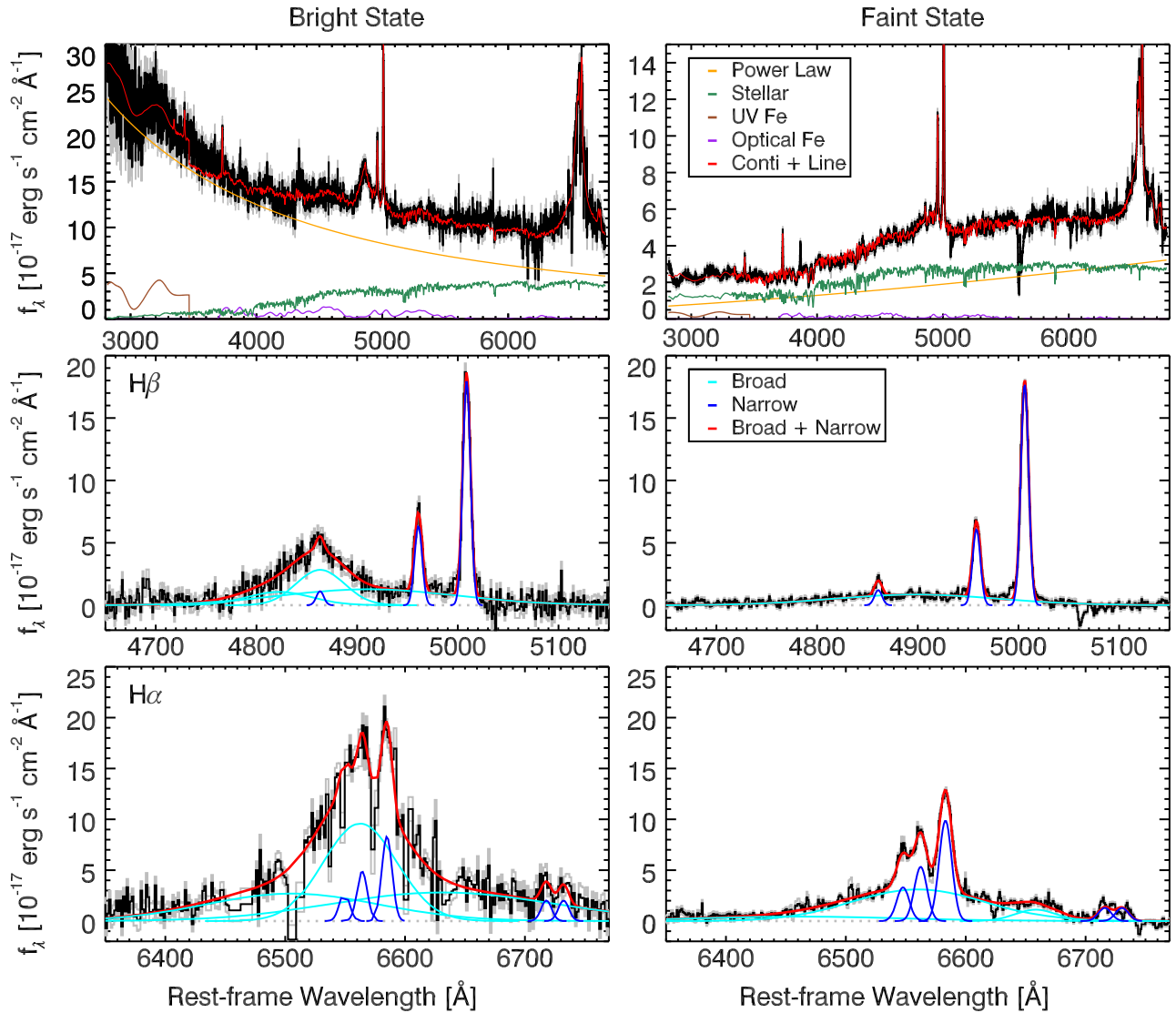


Figure 2. Optical spectral fitting to J0224, as an example, in the bright (left panels) and faint (right panels) states. The top panels show the decomposition of continuum emission, including AGN power-law (orange), host galaxy stellar (green), UV Fe II (brown), and optical Fe II (purple). The black and gray lines are the spectral flux densities (in units of $10^{-17} \text{ erg s}^{-1} \text{ cm}^{-2} \text{ \AA}^{-1}$) and their uncertainties. The red lines are the total models from the line emission and all of the continuum components described above. In the middle ($\text{H}\beta$) and bottom ($\text{H}\alpha$) panels, there are broad (cyan) and narrow (blue) emission line components.

observed X-ray spectrum is a result of the intrinsic spectrum modified by line-of-sight absorption, mainly from the intrinsic absorption at the quasar redshift and the Galactic absorption from the Milky Way. Therefore, we used the XSPEC model

$$\text{phabs} * \text{zphabs} * \text{zpower}, \quad (4)$$

where *phabs* is the Galactic absorption, *zphabs* models the intrinsic absorption with the redshift fixed to the source redshift, and *zpower* is a simple photon power law redshifted to the source redshift. We used the *nh* task in HEASOFT to obtain the Galactic absorption column density, N_{H} , derived from the H I map (Kalberla et al. 2005). The typical Galactic values of N_{H} for our CLQs are $2 \times 10^{20} \text{ cm}^{-2}$.

3.3. SED Fitting

We constructed SEDs for each object separately for the bright and faint states by using the photometric and spectroscopic measurements closest to those states. Since we are interested in the Eddington ratio in different states for these

accreting SMBHs, we calculate the bolometric luminosity, L_{bol} , by fitting to the SEDs. We use the X-CIGALE software (Yang et al. 2020a) version v2022.1. The X-CIGALE software implements a modern UV-to-IR AGN module, SKIRTOR (Stalevski et al. 2012, 2016), which is a clumpy torus model. Host galaxy stellar emission is also considered in X-CIGALE using the stellar population spectra of Bruzual & Charlot (2003).

To fit the X-ray data into the full SED fit across all wavelengths, X-CIGALE uses the UV-to-X-ray slope, i.e., α_{OX} . We use a definition of α_{OX} following the literature (e.g., Tananbaum et al. 1979; Lusso et al. 2010; Ruan et al. 2019; Jin et al. 2021) as

$$\alpha_{\text{OX}} = 0.3838 \log(L_{2500 \text{ \AA}} / L_{2 \text{ keV}}), \quad (5)$$

where $L_{2500 \text{ \AA}}$ and $L_{2 \text{ keV}}$ are the AGN intrinsic luminosities per frequency (in units of $\text{erg s}^{-1} \text{ Hz}^{-1}$) at 2500 Å (UV) and 2 keV (X-ray), respectively.

Since we have X-ray measurements as described in Section 3.2, we fixed the X-ray photon indices, Γ_X , and normalizations (fluxes) to the values measured from the X-ray spectra. To fit the full SED across undetected regions such as the extreme UV, X-CIGALE uses expected AGN values of $\alpha_{\text{OX}} = 0.137 \log(L_{2500 \text{ \AA}}) - 2.638$ (Just et al. 2007) within a specified tolerance. To explore a wide range of SED shapes and possible variability of α_{OX} , we allow for a large deviation, $|\Delta\alpha_{\text{OX}}|_{\text{max}} = 0.6$, from this relation. The calculated α_{OX} values are fairly robust to the fact that the photometric data and X-ray observations were not taken simultaneously. For example, a change of 30% in $L_{2500 \text{ \AA}}$ or $L_{2 \text{ keV}}$ leads to a difference of 0.04 in α_{OX} , which is comparable to the uncertainties for α_{OX} .

Galactic extinction correction is not implemented in X-CIGALE. For optical, NIR, and MIR data, we corrected the Galactic extinction for each band as described in Section 2.2.

4. Results

4.1. Optical Results

The optical spectroscopic observations demonstrate that the quasar continuum emission dimmed significantly, along with the broad Balmer emission. In all five CLQs, broad $H\beta$ and $H\gamma$ disappeared. In three CLQs, J0224, J1226, and J1338, there is visible broad $H\delta$ emission in the bright state that disappeared in the faint state. For two CLQs at lower redshift, and thus with coverage of $H\alpha$ emission, J0206 and J0224, the broad $H\alpha$ becomes weaker in the faint state but still remains visible (see the spectral fitting to J0224 in Figure 2). For the other three CLQs at higher redshift, and thus with coverage of Mg II, the broad Mg II emission decreases but remains visible as well. This phenomenon is consistent with previous spectroscopic follow-up of CLQs (e.g., Yang et al. 2018; MacLeod et al. 2019; Green et al. 2022).

We calculate the significance of the $H\beta$ change, defined in Equation (2). Four of the five CLQs vary at the $\gtrsim 4\sigma$ level, and one CLQ, J1338, the first one observed in 2017 that rapidly brightened again, shows a decrease of broad $H\beta$ slightly below the 3σ level.

MacLeod et al. (2019) and Green et al. (2022) used a criterion defining CLQ behavior as having a change of broad $H\beta$ flux at $N_\sigma(H\beta) \geq 3$. Green et al. (2022) suggested that additional intrinsic criteria less dependent on signal-to-noise ratio might be that the fractional change in both continuum luminosity and broad $H\beta$ line luminosity should be larger than 30%. In practice, nearly all CLQs that satisfy the $N_\sigma(H\beta) \geq 3$ criterion also satisfy the other two criteria. In Table 5, we summarize some of the relevant spectral fitting measurements. We measure the BEL luminosities (for $H\beta$, $H\alpha$, and Mg II) and rest-frame 3000 Å luminosities, $L_{3000 \text{ \AA}}$, in the bright and faint states. The BEL luminosities and $L_{3000 \text{ \AA}}$ change by more than 30% between the bright and faint states for all five CLQs.

Using the bright-state spectra with their prominent broad $H\beta$ emission, we find that the virial M_{BH} based on Equation (3) for these CLQs are $10^{8-9} M_\odot$ (see individual results in Table 5). Our M_{BH} measurements are consistent with the results in Wu & Shen (2022), though slightly lower (0.04–0.29 dex) because we accounted for the host galaxy contribution, thus yielding a lower AGN continuum emission.

Figures 3 and 4 show the multiwavelength light curves of the five new CLQs in the X-ray, optical g and r bands, and MIR

W1 and W2 bands (top to bottom). In the optical, the photometric data have been calibrated to the SDSS filter magnitude (as described in Section 2.2). The multiwavelength light curves show highly coordinated variability trends across the different wave bands.

The typical quasar variability is stochastic. In contrast, J1226 faded quite steadily for more than two decades, from 1999 to 2021, in all bands from X-ray to MIR. The light curves show that J1226 is different from the other four CLQs, which have shorter-timescale stochastic variability. Recent ZTF photometric data show signs of rebrightening in all five CLQs.

The Chandra observation shows J1338 to be brighter than its previous X-ray observation (described in Section 4.2). It brightened by 0.7 mag in the g band and 0.3 mag in the r band within 2 months from our MMT observation to the Chandra observation according to our photometric monitoring using the 1.2 m FLWO telescope. The r -band photometry close to the Chandra observation is actually 0.1 mag brighter than that close to the XMM-Newton observation. In the Magellan spectrum, 11 months after the MMT observation, the broad $H\beta$ line reappeared. Therefore, we remove J1338 in the analysis in Section 4.2, as our Chandra X-ray observation was not performed in its faint state.

4.2. X-Ray Results

Since the primary physical puzzles concern the SMBH accretion rate and intrinsic absorption, X-ray observations are the ideal probes. We first fit the X-ray spectra in both states independently. Figure 5 shows the X-ray spectral fitting results for the five CLQs in epochs 1 (left panels) and 2 (right panel) with the model described in Section 3.2. Within each panel, the observations taken for the same object with the same telescope within 1 week are fit together. The different colors/symbols are data from different observations (or cameras). We summarize the X-ray fitting results in Table 6.

No strong intrinsic absorption is detected in either the bright or faint states for these quasars. The faint-state X-ray spectra are well fit with zero intrinsic column density, $N_{\text{H,intrin}}$, with 1σ upper limits smaller than or comparable with the $N_{\text{H,intrin}}$ values in the bright-state X-ray spectra. This finding is consistent with previous X-ray studies of CLQs (LaMassa et al. 2015; Ai et al. 2020) and CL AGN such as Mrk 590 (Denney et al. 2014) and Mrk 1018 (Husemann et al. 2016).

Instead, we detected changes in the power-law continuum in both photon index and flux. Apart from J1338, which rebrightened rapidly, in the other four CLQs, the intrinsic fluxes in epoch 2 are lower than those in epoch 1. As shown in Figure 3, their X-ray emission generally changes together with the optical variability. The X-ray spectra are harder in the faint state, consistent with the trend in ensembles of AGN (e.g., Dong et al. 2014). As the energy range of Chandra (0.5–7 keV) is different from that of XMM-Newton (0.3–12 keV), we tested the spectral shape changes using the same energy range of 0.5–7 keV. Restricting the XMM-Newton fitting to the 0.5–7 keV energy range, the Γ_X values differ by $\lesssim 0.02$, which is much smaller than the typical uncertainty of Γ_X . Therefore, the conclusion of the X-ray spectrum change is not affected by the difference between the two energy ranges.

As X-ray data are sensitive to absorption, we use the X-ray spectra to test the changing-obscuration model. Assuming that varying absorption is the cause of the changes, we fix the AGN power-law continuum parameters in the faint state to

Table 5
Optical Spectroscopic Properties

Name	$N_\sigma(\text{H}\beta)$	$\log(L_{\text{H}\beta,1})$ erg s ⁻¹	$\log(L_{\text{H}\beta,2})$ erg s ⁻¹	$\log(L_{\text{H}\alpha,1})$ erg s ⁻¹	$\log(L_{\text{H}\alpha,2})$ erg s ⁻¹	$\log(L_{\text{MgII},1})$ erg s ⁻¹	$\log(L_{\text{MgII},2})$ erg s ⁻¹	$\log(L_{3000,1})$ erg s ⁻¹	$\log(L_{3000,2})$ erg s ⁻¹	$\log(\lambda L_{5100 \text{ \AA}})$ erg s ⁻¹	$\log(L_{[\text{O III}]})$ erg s ⁻¹	FWHM _{Hβ} km s ⁻¹	$\log(M_{\text{BH}})$ M_\odot	$\log(M_{\text{BH,ref}})$ M_\odot
J0206	3.59	42.32 ± 0.02	41.84 ± 0.12	43.04 ± 0.01	42.66 ± 0.01	42.24 ± 0.02	...	44.03 ± 0.01	43.70 ± 0.03	43.06 ± 0.01	42.14	9700 ± 500	8.90 ± 0.05	8.95 ± 0.04
J0224	5.85	42.50 ± 0.01	42.01 ± 0.02	43.04 ± 0.03	42.53 ± 0.02	44.38 ± 0.01	44.58 ± 0.01	43.14 ± 0.09	42.00	5100 ± 300	8.51 ± 0.05	8.74 ± 0.05
J0829	3.91	42.67 ± 0.05	42.20 ± 0.04	43.02 ± 0.01	42.14 ± 0.04	44.32 ± 0.02	44.52 ± 0.02	42.90 ± 0.02	41.55	3900 ± 800	8.25 ± 0.17	8.54 ± 0.13
J1226	4.41	43.07 ± 0.07	42.38 ± 0.03	43.48 ± 0.02	42.79 ± 0.01	44.60 ± 0.02	45.04 ± 0.02	43.67 ± 0.02	41.97	2900 ± 600	8.13 ± 0.15	8.17 ± 0.12
J1338	2.76	42.51 ± 0.08	42.17 ± 0.05	42.67 ± 0.05	44.24 ± 0.09	43.28 ± 1.06	41.57 ± 0.09	44.30 ± 0.05	41.85	4400 ± 700	8.34 ± 0.13	8.60 ± 0.15

Note. Here $N_\sigma(\text{H}\beta)$ is the significance of the change in H β broad-line emission between the bright and faint states; $L_{\text{H}\beta,1}$ and $L_{\text{H}\beta,2}$ are the broad H β line luminosities in the bright and faint state, respectively; $L_{5100 \text{ \AA}}$ is listed for the bright state only, as that is what we use to calculate M_{BH} ; $L_{[\text{O III}]}$ is the best-fit rescaled narrow [O III] $\lambda 5007$ line luminosity; and $M_{\text{BH,ref}}$ are the values derived by Wu & Shen (2022), shown for comparison.

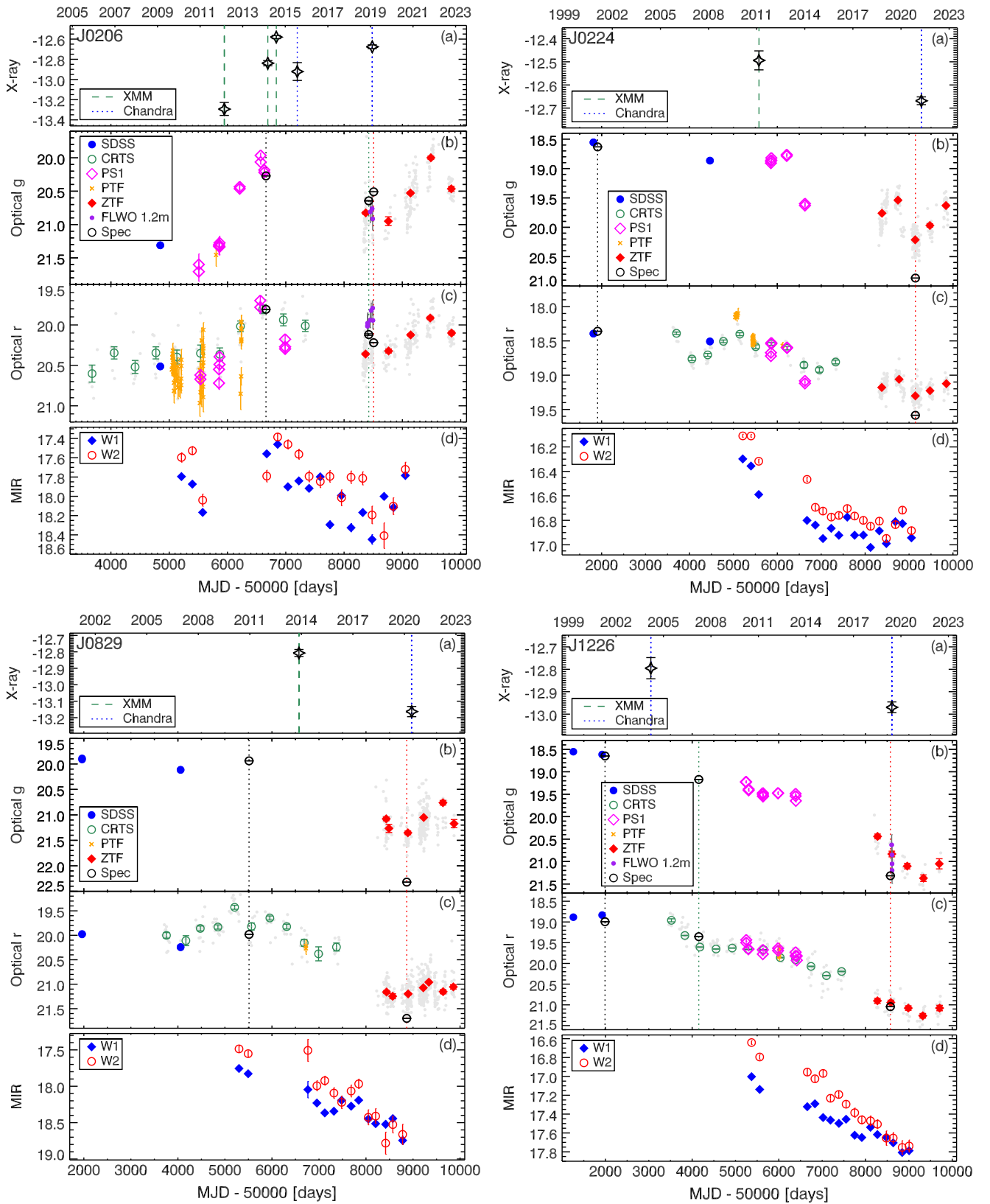


Figure 3. Light curves of the CLQs. The bottom X-axis is MJD – 50,000 days, and the X-axis across the top indicates the first date in each year. For each CLQ, the panels are (a) X-ray 0.5–7 keV flux ($\text{erg s}^{-1} \text{cm}^{-2}$) in logarithm, (b) optical *g*-band magnitude, (c) optical *r*-band magnitude, and (d) WISE MIR W1-band (blue) and W2-band (red) Vega magnitude. In panel (a), the vertical lines indicate the epochs of the X-ray observations, including XMM (green dashed) and Chandra (blue dotted). In panels (b) and (c), the different colors and symbols are from various optical imaging surveys, including SDSS (blue filled circles), CRTS (gray dots, with the mean for each year’s data as green open circles), PS1 (magenta open diamonds), PTF (orange crosses), ZTF (gray dots, with the mean for each year’s data as red filled diamonds), FLWO (purple dots), and synthetic photometry from spectra (black open circles). The vertical dotted lines indicate the epochs of the optical spectroscopic observations. The multiwavelength observations obviously show the same variability trend. Recent ZTF and/or FLWO data show signs of rebrightening.

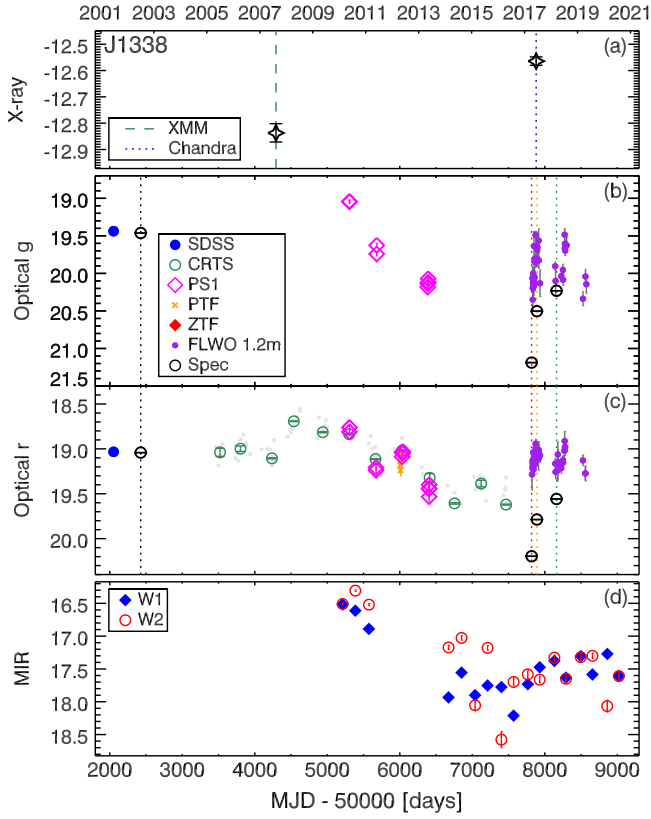


Figure 4. Same as Figure 3.

the measurements obtained in the bright state, with only quasar intrinsic column density as a free parameter. Figure 6 shows the results for the four CLQs observed in the faint state by Chandra. The plotted data are from Chandra in the faint state. The dotted black line is the independent best-fit model in the faint state. The dashed red line is the best-fit changing-obscuration model to the faint-state data. The results demonstrate that the changing-obscuration model does not match the observations. The reduced χ^2 value, $\chi^2_{\text{red,obsc}}$, of this changing-obscuration model is larger than the results of the independent best-fit model (summarized in Table 7). For these CLQs, the X-ray data are not consistent with a varying absorption scenario.

4.3. CLQ SED Variability

The CLQs show multiwavelength variability. Figure 7 illustrates the comparison between the SEDs in epochs 1 (black) and 2 (red). We fit the SEDs with components including an AGN (X-ray and UV-to-IR), host galaxy, and dusty torus (as described in Section 3.3). The bottom right panel shows an example of the SED decomposition for J1226 in the bright state. In four CLQs, J0206, J0224, J0829, and J1226, epoch 2 is fainter than epoch 1 throughout the electromagnetic spectrum. We integrate the best-fit SED model to obtain the bolometric luminosity, L_{bol} , and use the virial M_{BH} obtained from the optical spectra to calculate the Eddington ratio, λ_{Edd} . Only for J1338 is the L_{bol} higher in epoch 2 than in epoch 1. The L_{bol} values span $10^{44.7-45.6}$ erg s $^{-1}$, and the λ_{Edd} values range from $10^{-2.2}$ to $10^{-0.5}$ (0.6% to \sim 30%; summarized in Table 8). We also measure the UV luminosity ($\lambda_{2500 \text{ \AA}}$) and UV-to-X-ray slope (α_{OX}) from the SED fitting. Use of the SED fitting is more accurate for this purpose than

simply extrapolating rest-frame luminosities from the total observed fluxes because we are interested in changes to the AGN emission, and our SED fitting models the host galaxy and AGN components separately, which is especially important for the faint states.

The entire SED variability shape is not consistent with varying obscuration; while the MIR flux varies significantly, it is at most weakly affected by dust extinction. The extinction coefficient in the g band is a factor of >15 greater than that in the $W1$ band, according to the extinction law of Fitzpatrick (1999), across a range of R_V values (see Table A1). All five CLQs vary by more than 0.5 mag in the $W1$ band, which cannot be caused by changing extinction given the corresponding $\sim 1-2$ mag optical variability. Some of the CLQs show larger variability in the $W2$ band than in the $W1$ band, also inconsistent with an extinction model.

It is more likely that the changes in these CLQs are due to a changing accretion state of the SMBH, whereby the multi-wavelength emission varies accordingly. The accretion rate of the central SMBH decreased, so the whole system dimmed. The AGN emission throughout the entire electromagnetic spectrum—the UV-optical emission from the accretion disk, X-ray emission from the corona, and MIR emission from the reradiation in the dusty torus—decreased as the luminosity from the central engine decreased. As a consequence, the emission from the BLR, photoionized by the UV emission from the accretion disk, fades. The SEDs show stronger variability in the X-ray, UV-optical, and MIR than in the NIR. This is also reasonable in this scenario because the emission in the NIR is dominated by the host galaxy, which does not vary. If the common model of AGN structure with hotter regions at smaller radii is correct, then densely cadenced multiwavelength photometry throughout a state transition should verify that continuum changes generally propagate with time from shorter to longer wavelengths.

4.4. Dust Echoes in CLQs

If the MIR light is reprocessed light from the torus, its echo of the UV/optical continuum variations measures the average light-crossing time (hence a typical size) of the dust torus to the central engine. We measure the time lags between the MIR $W1$ -band and optical r -band light curves of these CLQs. We use the public code JAVELIN, which fits the light curves using a damped random walk (DRW) model and aligns them to recover the time lag (Zu et al. 2011). The DRW model has proven to be a reasonably good prescription to describe the optical continuum variability of quasars (e.g., Kelly et al. 2009; MacLeod et al. 2010). The inner boundary of the torus is thought to be set by dust sublimation at roughly ~ 1500 K; thus, the innermost region is mainly emitting in the NIR (e.g., Kishimoto et al. 2007). For the five CLQs with redshift at 0.36–0.64, the WISE $W1$ ($3.4 \mu\text{m}$) band probes the dust emission at rest frame $2.1-2.5 \mu\text{m}$. The MIR $W1$ -band emission has been used previously to measure the torus radii for quasars (e.g., Lyu et al. 2019; Yang et al. 2020b), while in nearby AGN, NIR K -band emission has been used (e.g., Suganuma et al. 2006; Koshida et al. 2014).

Robustly measuring the lag between two sets of light curves depends on the quality of the light curves (e.g., duration, cadence, signal-to-noise ratio), as well as their intrinsic variability (Yang et al. 2020b). To explore all possible lags while preserving significant overlaps between MIR and optical light curves, we allow a large lag search window of $[-1000, 2000]$ days. In

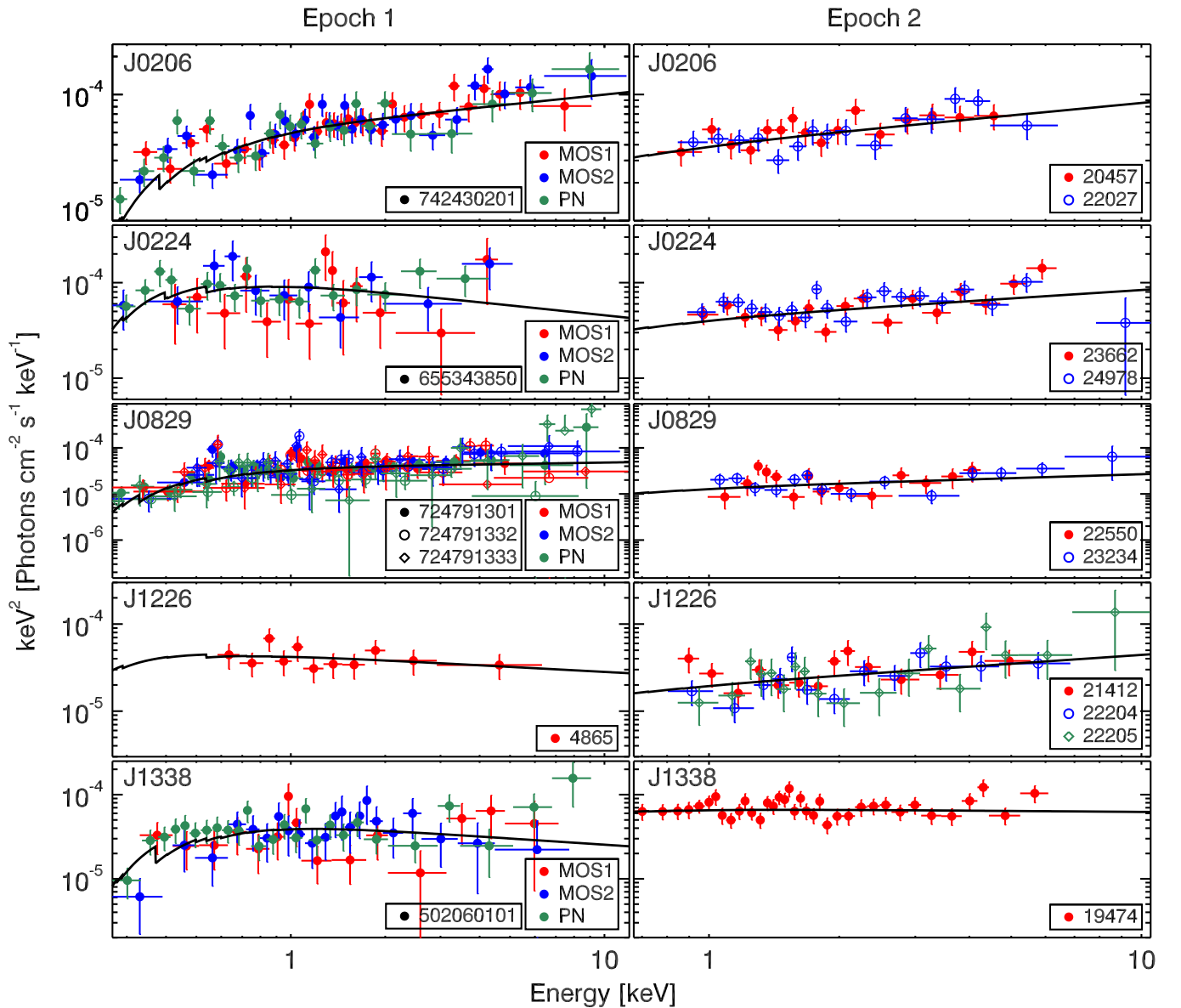


Figure 5. The X-ray spectra of the five CLQs. For each CLQ, the left panel is epoch 1, and the right panel is epoch 2. The black lines are the best-fit models. Different symbols are from different observations. The first four CLQs became fainter in epoch 2, consistent with the optical state. The last one, J1338, rebrightened quickly near the epoch of the Chandra follow-up (confirmed by the Magellan optical spectroscopic follow-up). No strong intrinsic absorption is detected in the faint state. Changes in the power-law continuum were detected in both the photon indices and the fluxes.

Figure 8, we show the lag measurement results for the five CLQs. We measure high-fidelity lags (with one primary lag peak) using JAVELIN for J1338 (166_{-19}^{+12} days) and J0829 (200_{-39}^{+29} days), consistent with the peak from the interpolated cross-correlation function (ICCF; Gaskell & Peterson 1987; Peterson et al. 1998). For J0224, we obtained a positive lag of 232_{-15}^{+14} days and a negative lag with lower probability. For J0206, the ICCF value is small (<0.5), and JAVELIN obtains two equal positive peaks at 179 and 299 days. Object J1226 faded all the way over two decades, so it is hard to measure to a time lag between the two light curves without an extreme value. As a consequence, as shown in the bottom right panel of Figure 8, the ICCF value of J1226 is large across the whole lag search window, and JAVELIN identifies too many alias peaks.

Figure 9 shows the correlation between the dusty torus size, inferred from the rest-frame IR lag, and the rest-frame

optical quasar luminosity.¹³ Yang et al. (2020b) measured a high-fidelity lag between the MIR and optical for a sample of 587 quasars at $\langle z \rangle \sim 0.8$. Among these quasars, seven were reported as CLQs (shown as orange filled diamonds), including four in MacLeod et al. (2016; J0023+0035, J2146+0009, J2252+0109, and J2333–0023), one in MacLeod et al. (2019; J2317+0114), one in Yang et al. (2020c; J2343+0038), and one in Green et al. (2022; J0212–0030). The dusty torus sizes of the two CLQs with high-fidelity lags (J0829 and J1338) and one CLQ using the primary positive lag (J0224), as well as the seven CLQs in the literature, are fully consistent with the torus R – L relation (Kishimoto et al. 2007), including the torus size measurements for nearby AGN (Suganuma et al. 2006;

¹³ To directly compare with earlier studies, following Yang et al. (2020b), we convert the bolometric luminosity to V -band luminosity (assuming a bolometric correction of 10 in the V band).

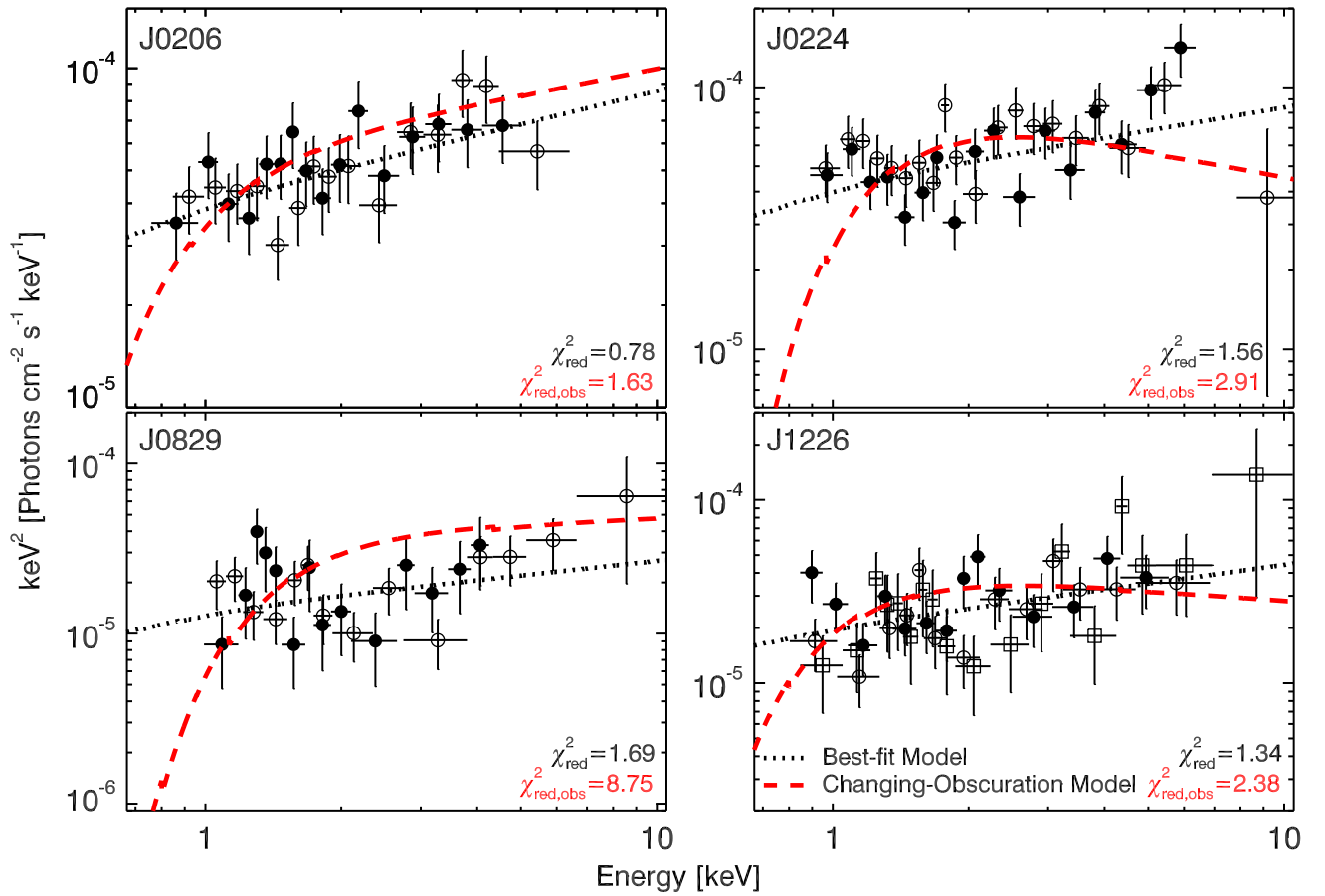


Figure 6. The X-ray spectral fitting for four CLQs in our Chandra X-ray faint-state observations (J1338 is not included). The different symbols refer to Chandra observations with different ObsIDs (filled circles, open circles, and open squares with observation times from early to late). The black dotted lines are the best-fit models to epoch 2 (faint-state) X-ray spectra. The red dashed lines are the changing-obscuration model fits to the epoch 2 spectra, assuming that the epoch 2 and 1 intrinsic spectra are identical with varying obscuration. The X-ray spectra are more consistent with intrinsic variation (both in Γ_X and flux), rather than the changing-obscuration model.

Koshida et al. 2014) and normal quasars (Lyu et al. 2019; Yang et al. 2020b). The MIR variability echoes the variability in the optical, with a time lag expected from the light-crossing time of the dusty torus.

5. Discussion

5.1. Fundamental Plane of BH Activity

Accretion onto BHs illuminates important physics from stellar mass BHs in XRBs to SMBHs. The fundamental plane of the BHs shows the correlation of radio luminosity, X-ray luminosity, and BH mass for hard-state XRBs and their supermassive analogs (e.g., Merloni et al. 2003; Falcke et al. 2004; Plotkin et al. 2012; Dong et al. 2014; Gültekin et al. 2019). The theoretical framework behind the fundamental plane typically assumes a BH fed by an RIAF that is launching a compact, partially self-absorbed synchrotron jet (implying unresolved radio emission with a flat/inverted spectrum; e.g., Heinz & Sunyaev 2003).

Using the VLA radio observations, we obtain the radio luminosity at 5 GHz in the rest frame, $L_{5\text{ GHz}}$, typically $\sim 10^{39}$ erg s^{-1} for the four CLQs (summarized in Table 4). In Figure 10, we plot the CLQs on the edge-on view of the fundamental plane in Merloni et al. (2003). The sources in black are QSOs (stars; Kaspi et al. 2000), Seyferts (circles), low-luminosity AGN in LINERs (triangles), XRBs (diamonds;

Merloni et al. 2003, and references therein), and Sgr A* and M32 (squares; Schödel et al. 2002; Verolme et al. 2002). The correlation extends over many decades in BH mass and luminosity, including many different sources, from stellar mass BHs to SMBHs. The CLQs appear to follow the fundamental plane relation. However, there are several caveats to bear in mind that complicate physical interpretations with current data. Foremost, although we detect radio emission from all four CLQ targets in their faint states, we stress that it is unclear if this emission is related to the activation of a compact jet or if the radio emission is instead a relic from the previous QSO phase. It is also unknown if our targets' radio emission has flat/inverted spectra, and only two of our targets remain unresolved at VLA spatial resolutions (J0224 and J1226). We use different symbols in Figure 10 to distinguish point sources (filled circles) and possible extended sources (filled diamonds).

5.2. Analogy between AGN and XRBs

Accretion state transitions have been detected in many XRBs. The X-ray power-law continuum slope correlates strongly with Eddington ratio, λ_{Edd} , in individual XRBs as their accretion state varies, such as Swift J1753.5–0127 (Cadolle Bel et al. 2007), H1743–322 (Jonker et al. 2010), and GX 339–4 (e.g., Corbel et al. 2013). Similar trends are seen (so far) across samples of quasars and Seyferts (e.g.,

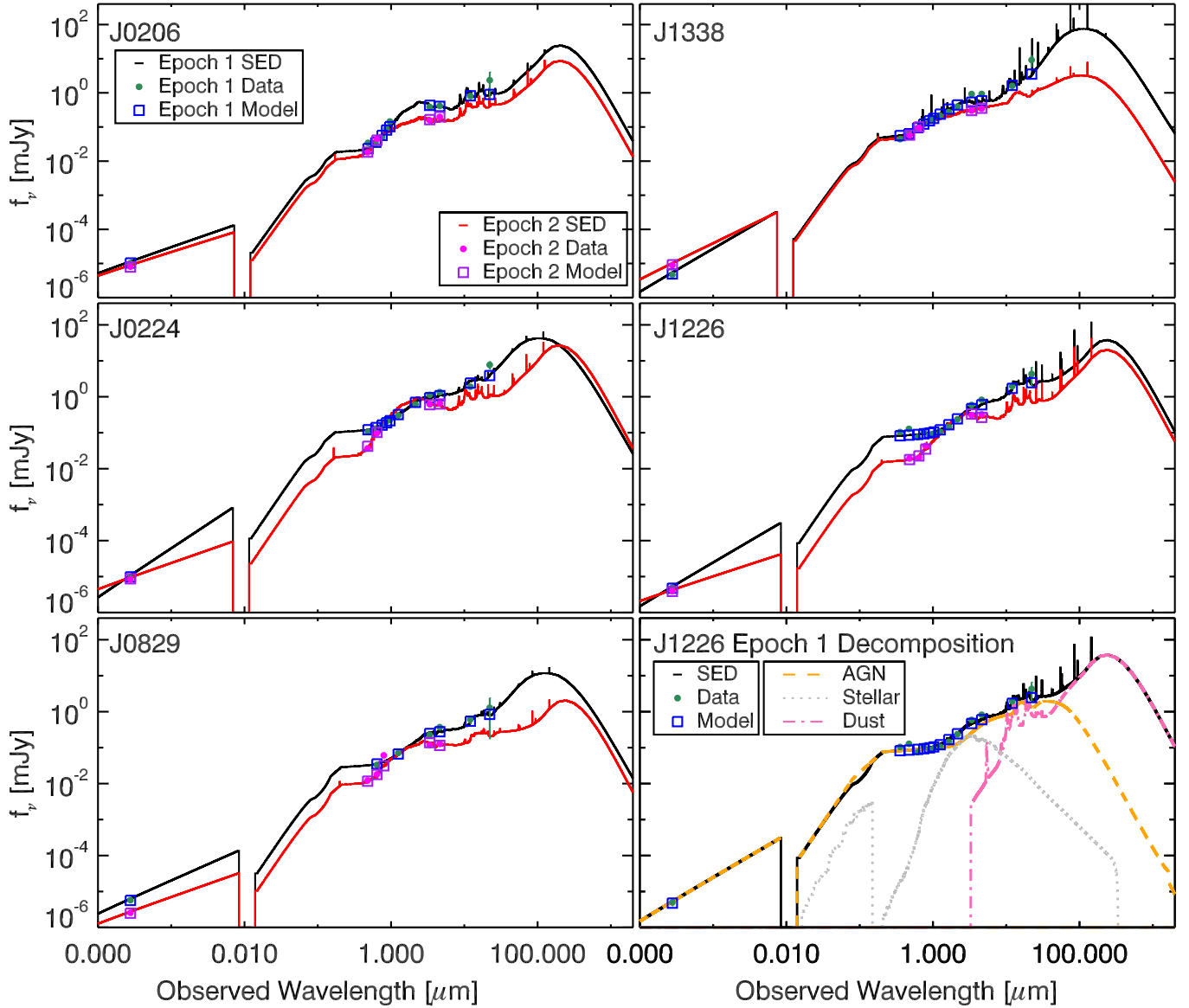


Figure 7. The SED fitting to the five CLQs. The solid lines are the best-fit SED models in epochs 1 (black) and 2 (red). The filled circles are the imaging observation data in epochs 1 (green) and 2 (magenta); also shown are the model fluxes in the corresponding bands in epochs 1 (blue) and 2 (purple). The bottom right panel shows an example of the SED decomposition of J1226 in epoch 1 consisting of components including AGN (orange dashed), host galaxy stellar emission with attenuated extinction (gray dotted), and a dusty torus (pink dashed-dotted). There is stronger variability in the X-ray, UV/optical, and MIR than in the NIR, which is dominated by host galaxy emission. The dramatic variability in the MIR and the trend of larger variability in the longer wavelengths are not consistent with the changing-obscuration model.

Trichas et al. 2013; Brightman et al. 2013) but have rarely been tracked in individual AGN, much less luminous quasars. Figure 11 shows the X-ray power-law slope, Γ_X , versus the Eddington ratio. The colored dots are our five CLQs; dots of the same color represent the same object in different states. The black filled squares are individual AGN in the sample of Dong et al. (2014), and the other black symbols are individual XRBs. Each individual CLQ follows the same softer-when-brighter trend, probably due to changes in the hot corona temperature or opacity (e.g., Petrucci et al. 2018; Middei et al. 2019).

There is variability in both the UV/optical and X-ray. The parameter α_{OX} provides a measurement of the ratio of disk to corona emission. A large α_{OX} corresponds to strong UV relative to X-rays (i.e., a soft SED). Figure 12 shows the behavior of α_{OX} versus Eddington ratio, λ_{Edd} . The gray symbols are CLQ measurements in the faint state (Ruan et al.

2019; Jin et al. 2021) and (ROSAT) X-ray upper limits in the bright state (lower limits in α_{OX} , shown with upward arrows). The black symbols are three known CLQs with X-ray measurements in both states, including J0159 (Ruan et al. 2019) and J2252 and J2333 (Jin et al. 2021).

There is some evidence that α_{OX} varies with λ_{Edd} in two branches around a critical Eddington ratio of $\sim 10^{-2}$ (1%; e.g., Ruan et al. 2019; Jin et al. 2021). When $\lambda_{Edd} \gtrsim 1\%$, as is the case for our CLQ observations, α_{OX} hardens (decreases) when λ_{Edd} decreases. By contrast, when $\lambda_{Edd} \lesssim 1\%$, α_{OX} softens (increases) when λ_{Edd} is smaller. While there is evidence to support this trend from ensembles of AGN each observed once, it is key to track the trends among individual AGN observed at different accretion rates because other factors—most importantly, SMBH mass and inclination angle—are obviously fixed across epochs for individual AGN. Our CLQs are mostly

Table 6
X-Ray Spectral Analysis

Name	Telescope	Epoch	χ^2	dof	χ^2_{red}	$N_{\text{H,intrin}}$ 10^{22} cm^{-2}	Γ_{X}	Norm. 10^{-5}	$\log(F_{0.5-7\text{keV}})$ $\text{erg s}^{-1} \text{ cm}^{-2}$	$\log(\nu L_{2 \text{ keV}})$ erg s^{-1}	$\log(L_{2-10 \text{ keV}})$ erg s^{-1}
J0206	XMM-Newton	1	132.39	85	1.56	$0.06^{+0.01}_{-0.01}$	$1.74^{+0.06}_{-0.06}$	$10.13^{+0.63}_{-0.58}$	$-12.58^{+0.02}_{-0.02}$	$43.79^{+0.01}_{-0.01}$	$44.08^{+0.02}_{-0.02}$
J0206	Chandra	2	22.65	29	0.78	$0.00^{+0.07}_{-0.00}$	$1.67^{+0.09}_{-0.08}$	$7.20^{+0.79}_{-0.63}$	$-12.68^{+0.02}_{-0.02}$	$43.66^{+0.02}_{-0.02}$	$43.98^{+0.03}_{-0.03}$
J0224	XMM-Newton	1	80.20	45	1.78	$0.04^{+0.03}_{-0.02}$	$2.34^{+0.17}_{-0.16}$	$20.61^{+2.65}_{-2.22}$	$-12.49^{+0.04}_{-0.04}$	$43.81^{+0.03}_{-0.03}$	$43.89^{+0.06}_{-0.06}$
J0224	Chandra	2	54.73	35	1.56	$0.00^{+0.03}_{-0.00}$	$1.71^{+0.09}_{-0.09}$	$7.20^{+0.73}_{-0.68}$	$-12.67^{+0.02}_{-0.02}$	$43.53^{+0.02}_{-0.02}$	$43.84^{+0.03}_{-0.03}$
J0829	XMM-Newton	1	273.54	170	1.61	$0.09^{+0.03}_{-0.03}$	$1.90^{+0.09}_{-0.08}$	$9.67^{+0.98}_{-0.88}$	$-12.81^{+0.02}_{-0.02}$	$44.05^{+0.02}_{-0.02}$	$44.29^{+0.02}_{-0.03}$
J0829	Chandra	2	45.52	27	1.69	$0.00^{+0.37}_{-0.00}$	$1.72^{+0.22}_{-0.12}$	$3.23^{+1.30}_{-0.55}$	$-13.16^{+0.03}_{-0.03}$	$43.63^{+0.04}_{-0.04}$	$43.93^{+0.04}_{-0.04}$
J1226	Chandra	1	5.10	8	0.64	$0.00^{+0.22}_{-0.00}$	$2.19^{+0.19}_{-0.19}$	$13.02^{+2.37}_{-2.06}$	$-12.80^{+0.05}_{-0.05}$	$44.10^{+0.04}_{-0.04}$	$44.23^{+0.07}_{-0.07}$
J1226	Chandra	2	61.52	46	1.34	$0.00^{+0.03}_{-0.00}$	$1.66^{+0.11}_{-0.11}$	$4.63^{+0.65}_{-0.58}$	$-12.97^{+0.02}_{-0.02}$	$43.80^{+0.03}_{-0.03}$	$44.13^{+0.03}_{-0.03}$
J1338	XMM-Newton	1	79.54	65	1.22	$0.11^{+0.04}_{-0.03}$	$2.25^{+0.16}_{-0.15}$	$10.38^{+1.56}_{-1.29}$	$-12.84^{+0.03}_{-0.04}$	$43.72^{+0.03}_{-0.03}$	$43.83^{+0.05}_{-0.05}$
J1338	Chandra	2	42.38	35	1.21	$0.00^{+0.04}_{-0.00}$	$2.04^{+0.07}_{-0.07}$	$14.55^{+1.05}_{-1.01}$	$-12.56^{+0.02}_{-0.02}$	$43.93^{+0.02}_{-0.02}$	$44.11^{+0.03}_{-0.03}$

Note. Here $N_{\text{H,intrin}}$ is the best-fit intrinsic absorption column density at the quasar redshift in units of 10^{22} cm^{-2} .

Table 7
Changing-obscuration Model

Name	χ^2	dof	χ^2_{red}	χ^2_{abs}	dof _{abs}	$\chi^2_{\text{red,obsc}}$	$N_{\text{H,obsc}}$ 10^{22} cm^{-2}
J0206	22.653	29	0.78	50.394	31	1.63	$0.42^{+0.10}_{-0.09}$
J0224	54.727	35	1.56	107.572	37	2.91	$1.15^{+0.12}_{-0.11}$
J0829	45.523	27	1.69	253.722	29	8.75	$2.61^{+0.29}_{-0.29}$
J1226	61.520	46	1.34	114.350	48	2.38	$1.17^{+0.16}_{-0.17}$

Note. Here $\chi^2_{\text{red,obsc}}$, the reduced χ^2 value of the changing-obscuration model, is larger than the χ^2_{red} of the independent best-fit model from Table 6.

Table 8
SED Fitting Results

Name	State	$\log(L_{\text{bol}})$ erg s^{-1}	$\log(\lambda_{\text{Edd}})$	$\log(\lambda L_{2500 \text{ \AA}})$ erg s^{-1}	α_{OX}
J0206	1	44.94 ± 0.03	-2.06 ± 0.06	44.02 ± 0.06	1.10 ± 0.03
J0206	2	44.81 ± 0.03	-2.19 ± 0.06	43.80 ± 0.09	1.07 ± 0.03
J0224	1	45.26 ± 0.05	-1.35 ± 0.07	44.63 ± 0.07	1.29 ± 0.03
J0224	2	44.78 ± 0.03	-1.83 ± 0.06	43.93 ± 0.10	1.16 ± 0.04
J0829	1	45.32 ± 0.04	-1.04 ± 0.17	44.60 ± 0.06	1.22 ± 0.02
J0829	2	44.90 ± 0.02	-1.46 ± 0.17	44.11 ± 0.01	1.21 ± 0.02
J1224	1	45.64 ± 0.01	-0.59 ± 0.15	45.03 ± 0.01	1.35 ± 0.03
J1224	2	45.11 ± 0.02	-1.11 ± 0.15	44.33 ± 0.03	1.23 ± 0.02
J1338	1	45.15 ± 0.03	-1.29 ± 0.13	44.51 ± 0.03	1.28 ± 0.02
J1338	2	45.17 ± 0.05	-1.27 ± 0.14	44.44 ± 0.08	1.19 ± 0.03

$\lambda_{\text{Edd}} \gtrsim 1\%$, so the individual CLQs vary such that α_{OX} increases (softens) with λ_{Edd} . With a λ_{Edd} slightly lower than 10^{-2} , J0206 also follows this trend. Object J1338 is an outlier, but as we mentioned, it varies quickly, and we did not catch the desired faint state in X-rays. For J0159, with one epoch at $\lambda_{\text{Edd}} > 10^{-2}$ and another epoch at $\lambda_{\text{Edd}} < 10^{-2}$, LaMassa et al. (2015) reported no detected change in X-ray slope or (albeit with large errors) α_{OX} .

In Figure 12, the asterisks are predictions for AGN from Sobolewska et al. (2011) based on modeling the observed

X-ray spectral evolution of the XRB GRO J1655–40 during its accretion state transition and scaling the SED evolution up to AGN SMBH masses. The predicted data from XRBs also show a critical Eddington ratio of about 1%. The analogy of SMBHs and stellar mass BHs motivates a theoretical model to explain the phenomena. Referring to theoretical models of XRBs, Ruan et al. (2019) suggested that at high Eddington ratios, accretion proceeds via a geometrically thin accretion disk (Shakura & Sunyaev 1973). As λ_{Edd} decreases, there is less UV emission from the thin disk with a lower apparent temperature, so α_{OX}

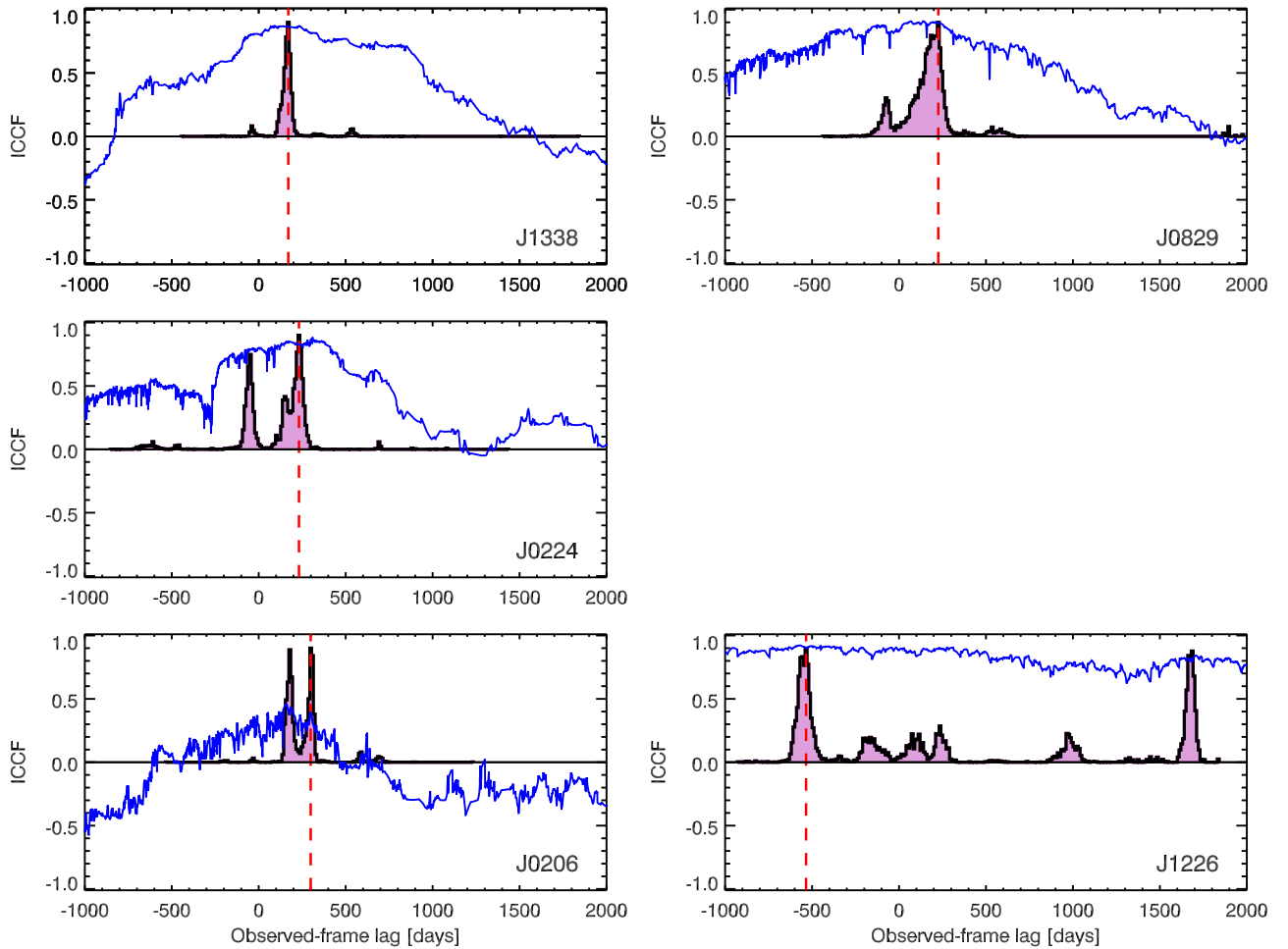


Figure 8. Time lag measurements between the WISE W1-band and optical r -band light curves. The blue solid line is the ICCF. The purple histogram (with black solid outline) shows the JAVELIN posterior lag distribution in the observed frame. The vertical red dashed line shows the primary peak of the JAVELIN posterior distribution. The top two panels show the two CLQs with high-fidelity lag measurements, J1338 (left) and J0829 (right). The middle panel shows one CLQ, J0224, with a marginal lag measurement, with one positive primary peak and one negative lag with lower probability. In the bottom panels, either the JAVELIN or ICCF algorithm fails to measure a robust MIR lag for J0206 (low ICCF value) and J1226 (many aliases).

decreases. When the λ_{Edd} is lower than 1%, a jet may be launched, or the inner region of the thin disk may progressively evaporate into a hot RIAF that is possibly advection-dominated (Narayan & Yi 1994). Thus, α_{OX} increases again, possibly due to the emergence of UV emission from either a jet or an advection-dominated accretion flow. For our CLQs, the λ_{Edd} is not far below 10^{-2} , and the radio-loudness is $\sim 10^{-5}$ (see Table 4), indicating no powerful jet launch, so our observations are consistent with the models. Multiepoch observations of CLQs at even lower Eddington ratios are warranted. The analogy with XRBs may break down at very low λ_{Edd} ; weak AGN in LINERs were found with $\lambda_{\text{Edd}} < 10^{-4}$ and $\alpha_{\text{OX}} \approx 1 \pm 0.1$ (Eracleous et al. 2010). However, the evidence so far indicates that most AGN with $\lambda_{\text{Edd}} < 1\%$ will not show BELs, so the necessary observations may require following significant intrinsic (i.e., not absorption-related) variability in type 2 AGN. In highly obscured type 2 AGN, even when there is strong variability in the MIR (>3 mag), the optical continuum emission could be highly obscured, preventing significant optical (<0.2 mag) or BEL variability (Yang et al. 2019). Strong variability in “naked type 2” AGN is relatively rare but worth pursuing; on closer inspection, they may be found to have weak broad $\text{H}\beta$ emission and/or broad $\text{H}\alpha$ (e.g.,

associated with types 1.8 or 1.9; Barth et al. 2014; López-Navas et al. 2022).

6. Summary

We present multiwavelength, multiepoch observations of five new CLQs and analyze the data in both the bright and faint states. Our main conclusions are as follows.

1. Our optical spectroscopic follow-up confirms CLQ behavior with continuum emission dramatically dimming accompanied by fading of broad Balmer emission lines, such as $\text{H}\beta$, $\text{H}\gamma$, and $\text{H}\delta$. By selection, their broad $\text{H}\beta$ varies at a $\gtrsim 3\sigma$ level. The broad $\text{H}\alpha$ and Mg II emission varies less (or more slowly) than $\text{H}\beta$.
2. The continuum emission from CLQs varies across the electromagnetic spectrum, in the X-ray, optical, and MIR.
3. The intrinsic X-ray continuum strength changes together with the optical continuum strength. The X-ray power-law slope changes following a harder-when-fainter trend. No strong absorption is detected in the faint-state X-ray spectra, so that a changing-obscuration model does not match the X-ray observations.

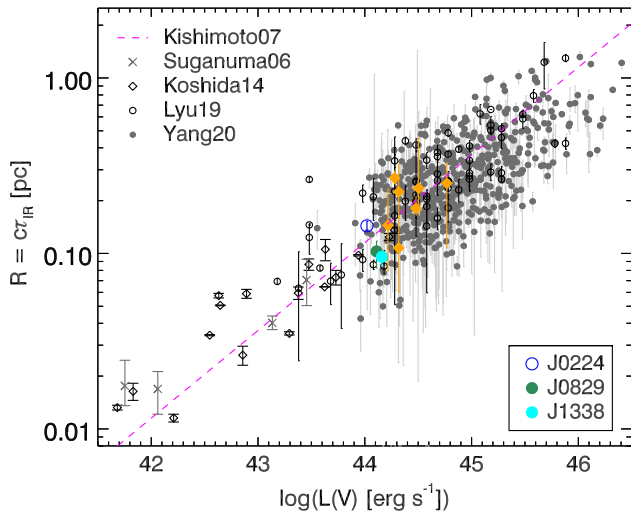


Figure 9. Dusty torus size inferred from the rest-frame IR lag vs. rest-frame optical quasar luminosity. The black diamonds and gray crosses are the lag measurements between the K and optical bands for nearby AGN (Suganuma et al. 2006; Koshida et al. 2014). The black open circles and gray dots are the lag measurements between the WISE $W1$ and optical bands for PG (Lyu et al. 2019) and SDSS (Yang et al. 2020b) quasars. The orange filled diamonds are the lag measurements in Yang et al. (2020b) for CLQs in the literature. The blue open, green filled, and cyan filled symbols are the lag measurements for CLQs in this work for J0224, J0829, and J1338, respectively. The magenta line is the radius-luminosity relation in Kishimoto et al. (2007).

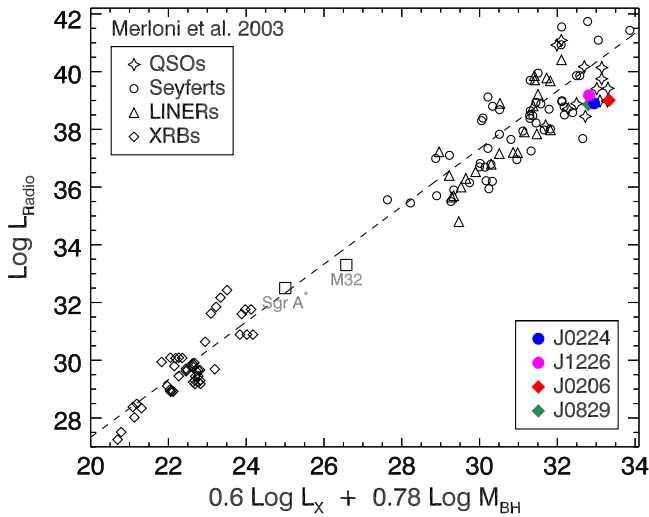


Figure 10. Edge-on view of the fundamental plane of BH activity. The sources in black are from Merloni et al. (2003), including QSOs (stars), Seyferts (circles), low-luminosity AGN in LINERs (triangles), XRBs (diamonds), and Sgr A* and M32 (squares). The colored symbols are the four CLQs observed by the VLA in the faint state, with filled circles denoting sources with unresolved radio emission and filled diamonds denoting extended radio emission.

4. The large-amplitude MIR variability (>0.5 mag) detected in all five quasars is also inconsistent with the changing-obscuration model.
5. The MIR variability for CLQs follows the variability in the optical, with a time lag consistent with the typical light-crossing time of the dusty torus for QSOs with robust lag measurements.
6. It is highly likely that the changes in these CLQs are due to the changing accretion rate of the SMBH, so the multiwavelength emission varies accordingly.

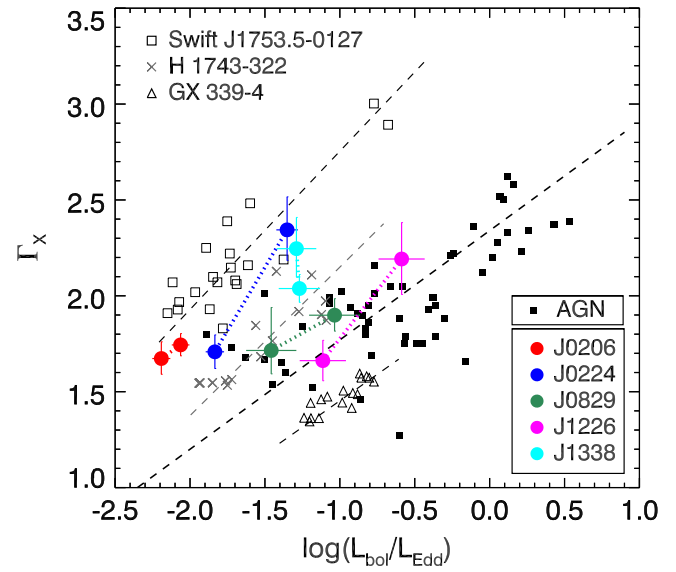


Figure 11. Relation between X-ray photon index, Γ_x , and Eddington ratio (L_{bol}/L_{Edd}) in logarithm for AGN and XRBs. The colored dots are our five CLQs, including J0206 (red), J0224 (blue), J0829 (green), J1226 (magenta), and J1338 (cyan). The dotted lines connect the CLQs in the bright and faint states. The black filled squares are measurements from AGN in Dong et al. (2014). There are some individual XRBs, including Swift J1753.5–0127 (open square), H1743–322 (cross), and GX 339–4 (open triangle). One can see the same softer-when-brighter trend in the AGN and XRBs. The individual CLQs follow this trend well. Unfortunately, J1338 was not captured in its faint state during our Chandra observation.

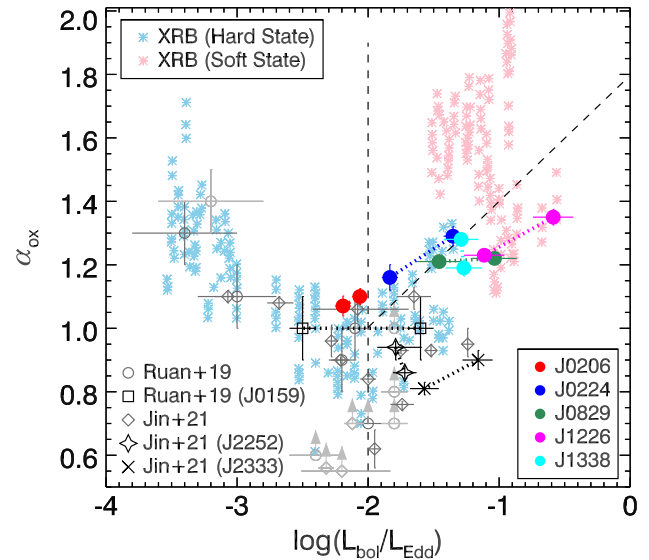


Figure 12. Relation between the UV-to-X-ray spectral index (α_{OX}) and the logarithm of the Eddington ratio $\log(L_{bol}/L_{Edd})$ for the AGN and XRBs. Both α_{OX} and L_{bol} are taken from our SED fitting. Colored dots indicate our five Chandra CLQs as in Figure 11. The gray symbols are from CLQs in the faint states (open circles) and lower limits in the bright states (open circles with arrows) in Ruan et al. (2019) and CLQs in the faint states (open diamonds) and lower limits in the bright states (open diamonds with arrows) in Jin et al. (2021). The black symbols are CLQs with X-ray observations in both states for J0159 (squares) analyzed in Ruan et al. (2019) and J2252 (stars) and J2333 (crosses) in Jin et al. (2021). The dotted line connects one CLQ observed in two states. The asterisks show results from the Galactic XRB GRO J1655–40 (Sobolewska et al. 2011) in the hard (sky blue) and soft (pink) states, extrapolated via mass scaling to type 1 AGN (see their Figure 4).

7. There are many similarities between the behavior of these CLQs and XRBs, indicating similarities in the BH accretion spanning factors of 10^8 in mass between stellar mass BHs and SMBHs.

Only a handful of CLQs have been observed in X-rays both before and after the state transition. More such observations are needed to characterize their behavior more generally. Our five CLQs are basically at $\lambda_{\text{Edd}} \gtrsim 10^{-2}$. More CLQ transitions over a wide range of λ_{Edd} will be important for studies of BH accretion processes and AGN structure.

Acknowledgments

We thank the referee for useful comments that improved the manuscript. We thank Ruancun Li and Malgorzata Sobolewska for useful discussions and suggestions. We thank Sebastian Gomez for help with observations and data reduction of the Magellan spectrum.

This research has made use of data obtained from the Chandra Data Archive and Chandra Source Catalog and software provided by the Chandra X-ray Center (CXC) in the application packages CIAO and Sherpa. Q.Y. was partially supported for this work by the National Aeronautics and Space Administration through Chandra award Nos. GO9-20086X and GO0-21084X, issued by the Chandra X-ray Center, which is operated by the Smithsonian Astrophysical Observatory for and on behalf of the National Aeronautics and Space Administration under contract NAS8-03060.

R.M.P. acknowledges support from the National Science Foundation under grant No. 2206123.

This work used observations obtained with XMM-Newton. Based on observations obtained with XMM-Newton, an ESA science mission with instruments and contributions directly funded by ESA Member States and NASA.

We acknowledge the use of telescopes including MMT, Gemini, Magellan, the 3.5 m telescope at APO, and the 1.2 m telescope at the Fred Lawrence Whipple Observatory, operated by the Smithsonian Institution. The observations reported here were obtained at the MMT Observatory, a joint facility of the Smithsonian Institution and the University of Arizona. Based on observations obtained at the international Gemini Observatory, a program of NSF's NOIRLab, which is managed by the Association of Universities for Research in Astronomy (AURA) under a cooperative agreement with the National Science Foundation on behalf of the Gemini Observatory partnership: the National Science Foundation (United States), National Research Council (Canada), Agencia Nacional de Investigación y Desarrollo (Chile), Ministerio de Ciencia, Tecnología e Innovación (Argentina), Ministério da Ciência, Tecnologia, Inovações e Comunicações (Brazil), and Korea Astronomy and Space Science Institute (Republic of Korea). This paper includes data gathered with the 6.5 m Magellan Telescopes located at Las Campanas Observatory, Chile. The Hobby–Eberly Telescope Board of Directors approved the following update to the HET's Publication Policy in fall 2023. All publications that include HET data are expected to comply with the policy, which involves acknowledgments of the telescope and instrumentation and appropriate citations of supporting publications. When a peer-reviewed paper using HET data appears in print, the lead author should contact the HET Publications Coordinator, currently Donald Schneider (dps7@psu.edu), with the final journal reference information. Based on observations obtained with the Apache Point Observatory 3.5 m telescope, which is owned and operated by the Astrophysical Research Consortium.

We acknowledge the use of SDSS data. Funding for SDSS-III has been provided by the Alfred P. Sloan Foundation, the

Participating Institutions, the National Science Foundation, and the US Department of Energy Office of Science. The SDSS-III website is <http://www.sdss3.org/>. The SDSS-III is managed by the Astrophysical Research Consortium for the Participating Institutions of the SDSS-III Collaboration, including the University of Arizona, the Brazilian Participation Group, Brookhaven National Laboratory, Carnegie Mellon University, the University of Florida, the French Participation Group, the German Participation Group, Harvard University, the Instituto de Astrofísica de Canarias, the Michigan State/Notre Dame/JINA Participation Group, Johns Hopkins University, Lawrence Berkeley National Laboratory, the Max Planck Institute for Astrophysics, the Max Planck Institute for Extraterrestrial Physics, New Mexico State University, New York University, Ohio State University, Pennsylvania State University, the University of Portsmouth, Princeton University, the Spanish Participation Group, the University of Tokyo, the University of Utah, Vanderbilt University, the University of Virginia, the University of Washington, and Yale University.

This research has made use of PS1, WISE, CRTS, and PTF imaging data. The PS1 has been made possible through contributions by the Institute for Astronomy, the University of Hawaii, the Pan-STARRS Project Office, the Max Planck Society and its participating institutes, the Max Planck Institute for Astronomy, Heidelberg, and the Max Planck Institute for Extraterrestrial Physics, Garching, The Johns Hopkins University, Durham University, the University of Edinburgh, Queen's University Belfast, the Harvard-Smithsonian Center for Astrophysics, the Las Cumbres Observatory Global Telescope Network Incorporated, the National Central University of Taiwan, the Space Telescope Science Institute, the National Aeronautics and Space Administration under grant No. NNX08AR22G issued through the Planetary Science Division of the NASA Science Mission Directorate, the National Science Foundation under grant No. AST-1238877, the University of Maryland, and Eotvos Lorand University (ELTE). This publication makes use of data products from the Wide-field Infrared Survey Explorer, which is a joint project of the University of California, Los Angeles, and the Jet Propulsion Laboratory/California Institute of Technology, funded by the National Aeronautics and Space Administration. The Catalina Sky Survey (CSS) is funded by the National Aeronautics and Space Administration under grant No. NNG05GF22G issued through the Science Mission Directorate Near-Earth Objects Observations Program. The CRTS survey is supported by the US National Science Foundation under grants AST-0909182 and AST-1313422. We acknowledge the use of PTF data, and the website is <https://www.ptf.caltech.edu>.

We acknowledge the use of ZTF data. Based on observations obtained with the 48 inch Samuel Oschin Telescope and the 60 inch telescope at the Palomar Observatory as part of the Zwicky Transient Facility project. The ZTF is supported by the National Science Foundation under grant No. AST-2034437 and a collaboration including Caltech, IPAC, the Weizmann Institute for Science, the Oskar Klein Center at Stockholm University, the University of Maryland, Deutsches Elektronen-Synchrotron and Humboldt University, the TANGO Consortium of Taiwan, the University of Wisconsin at Milwaukee, Trinity College Dublin, Lawrence Livermore National Laboratories, and IN2P3, France. Operations are conducted by COO, IPAC, and UW.

Facilities: Chandra, XMM-Newton, MMT (Blue Channel spectrograph, BinoSpec), Magellan:Baade (IMACS), Gemini (GMOS-N), APO 3.5 m (DIS), FLWO:1.2 m, Sloan, PS1, PTF, CRTS, ZTF, WISE.

Software: CIAO, SAS, XSPEC, CASA, IRAF, QSOFIT, X-CIGALE.

Appendix A Extinction Coefficient

We provide a table of conversion coefficients from $E(B - V)_{\text{SFD}}$ to extinction in 35 filters for the surveys we used in this work in Table A1. We calculated the extinction coefficients following the procedures in Schlafly &

Finkbeiner (2011). The extinction in band b is expressed as

$$A_b = -2.5 \log \left[\frac{\int d\lambda W_b(\lambda) S(\lambda) 10^{-A(\lambda) \Delta m_{1\mu\text{m}}/2.5}}{\int d\lambda W(\lambda) S(\lambda)} \right], \quad (\text{A1})$$

where $W_b(\lambda)$ is the filter throughput curve in band b as a function of wavelength λ , S is the source spectrum, A is the extinction law (Fitzpatrick 1999) normalized to $A_{1\mu\text{m}} = 1$, and $\Delta m_{1\mu\text{m}}$ is a normalization $N = 0.78$ times the extinction at $1\mu\text{m}$ according to Schlegel et al. (1998). The source spectrum S is a synthetic stellar spectrum with $T_{\text{eff}} = 7000$ K, $\log Z = -1$, and $\log g = 4.5$ from Munari et al. (2005; 2500–10500 Å) extrapolating into the infrared following a blackbody spectrum $S(\lambda) \propto \lambda^{-3}$. We compute the extinction coefficients $A_b/E(B - V)$, with $R_V = 2.1, 3.1, 4.1, \text{ and } 5.1$.

Table A1
Extinction Coefficients

Survey	Band	$A_b/E(B - V)$			
		$R_V = 2.1$	$R_V = 3.1$	$R_V = 4.1$	$R_V = 5.1$
SDSS	<i>u</i>	5.443	4.247	3.716	3.418
SDSS	<i>g</i>	3.852	3.304	3.052	2.907
SDSS	<i>r</i>	2.260	2.287	2.298	2.305
SDSS	<i>i</i>	1.585	1.697	1.749	1.780
SDSS	<i>z</i>	1.211	1.263	1.286	1.300
PS1	<i>g</i>	3.666	3.188	2.967	2.840
PS1	<i>r</i>	2.254	2.278	2.288	2.294
PS1	<i>i</i>	1.569	1.682	1.733	1.763
PS1	<i>z</i>	1.259	1.323	1.352	1.369
PS1	<i>y</i>	1.087	1.104	1.111	1.116
PTF	<i>g</i>	3.812	3.280	3.035	2.893
PTF	<i>R</i>	2.002	2.087	2.126	2.148
ZTF	<i>g</i>	3.748	3.240	3.005	2.870
ZTF	<i>r</i>	2.111	2.169	2.195	2.210
ZTF	<i>i</i>	1.444	1.542	1.587	1.612
FLWO	<i>g</i>	3.758	3.245	3.008	2.871
FLWO	<i>r</i>	2.226	2.254	2.266	2.273
FLWO	<i>i</i>	1.524	1.631	1.680	1.708
2MASS	<i>J</i>	0.778	0.722	0.696	0.681
2MASS	<i>H</i>	0.517	0.457	0.430	0.414
2MASS	<i>K_s</i>	0.344	0.308	0.292	0.282
UKIRT	<i>Z</i>	1.226	1.282	1.308	1.323
UKIRT	<i>Y</i>	0.989	0.978	0.973	0.970
UKIRT	<i>J</i>	0.765	0.707	0.680	0.664
UKIRT	<i>H</i>	0.524	0.464	0.437	0.421
UKIRT	<i>K</i>	0.335	0.301	0.285	0.276
VISTA	<i>Z</i>	1.247	1.307	1.335	1.352
VISTA	<i>Y</i>	1.003	0.996	0.993	0.991
VISTA	<i>J</i>	0.763	0.705	0.678	0.662
VISTA	<i>H</i>	0.520	0.461	0.433	0.417
VISTA	<i>K_s</i>	0.351	0.314	0.298	0.288
WISE	<i>W1</i>	0.180	0.176	0.174	0.173
WISE	<i>W2</i>	0.112	0.120	0.123	0.125
WISE	<i>W3</i>	0.034	0.046	0.052	0.055
WISE	<i>W4</i>	0.014	0.022	0.026	0.028

Appendix B

SED Data

We compiled the multiwavelength photometric data in both states (summarized in Table B1). Since we simultaneously fit

the X-ray to MIR SED, we chose the photometric data closest in time to the X-ray epochs (indicated by the “Epoch” column in Table 3).

Table B1
Photometric Data for CLQ SED













Name	Epoch	Survey/Telescope	Band	MJD	Mag.	Uncertainty
J0206	1	PS1	<i>g</i>	56,631.333	20.125	0.040
J0206	1	PS1	<i>r</i>	56,988.307	20.209	0.062
J0206	1	PS1	<i>i</i>	56,916.486	19.685	0.038
J0206	1	PS1	<i>z</i>	56,644.232	19.047	0.039
J0206	1	PS1	<i>y</i>	56,517.627	18.521	0.037
J0206	1	WISE	W1	56,860.281	14.762	0.019
J0206	1	WISE	W2	56,860.281	14.046	0.041
J0206	1	WISE	W3	55,312.068	11.487	0.134
J0206	1	WISE	W4	55,312.068	8.877	0.775
J0206	2	FLWO	<i>g</i>	58,481.133	20.816	0.100
J0206	2	FLWO	<i>r</i>	58,465.266	19.815	0.046
J0206	2	WISE	W1	58,480.006	15.748	0.051
J0206	2	WISE	W2	58,480.006	14.855	0.092
J0224	1	PS1	<i>g</i>	55,854.412	18.906	0.019
J0224	1	PS1	<i>r</i>	55,854.462	18.655	0.015
J0224	1	PS1	<i>i</i>	56,209.550	18.489	0.013
J0224	1	PS1	<i>z</i>	55,583.258	18.118	0.017
J0224	1	PS1	<i>y</i>	55,584.260	18.035	0.050
J0224	1	VHS	<i>J</i>	56,298.146	16.793	0.009
J0224	1	VHS	<i>K_s</i>	56,298.136	15.108	0.011
J0224	1	WISE	W1	55,213.406	13.599	0.009
J0224	1	WISE	W2	55,213.406	12.771	0.014
J0224	1	WISE	W3	55,318.732	10.551	0.052
J0224	1	WISE	W4	55,322.150	7.589	0.220
J0224	2	ZTF	<i>g</i>	59,138.359	20.058	0.025
J0224	2	ZTF	<i>r</i>	59,158.345	18.976	0.009
J0224	2	WISE	W1	59,054.290	14.244	0.013
J0224	2	WISE	W2	59,054.290	13.546	0.030
J0829	1	PTF	<i>r</i>	56,724.155	20.166	0.119
J0829	1	UHS	<i>J</i>	56,066–57,784	18.356	0.073
J0829	1	WISE	W1	56,764.247	15.347	0.114
J0829	1	WISE	W2	56,764.247	14.168	0.153
J0829	1	WISE	W3	55,299.743	11.789	0.228
J0829	1	WISE	W4	55,299.743	9.536	0.929
J0829	2	ZTF	<i>g</i>	58,891.198	21.285	0.036
J0829	2	ZTF	<i>r</i>	58,891.290	20.826	0.025
J0829	2	ZTF	<i>i</i>	58,257.172	19.485	0.108
J0829	2	WISE	W1	58,778.937	16.046	0.058
J0829	2	WISE	W2	58,778.937	15.322	0.138
J1226	1	SDSS	<i>u</i>	51,923	18.936	0.042
J1226	1	SDSS	<i>g</i>	51,923	18.699	0.021
J1226	1	SDSS	<i>r</i>	51,923	19.262	0.036
J1226	1	SDSS	<i>i</i>	51,923	18.822	0.027
J1226	1	SDSS	<i>z</i>	51,923	19.078	0.094
J1226	1	UKIDSS	<i>Y</i>	54,398	18.387	0.047
J1226	1	UKIDSS	<i>J</i>	54,398	17.772	0.054
J1226	1	UKIDSS	<i>H</i>	54,398	17.135	0.043
J1226	1	UKIDSS	<i>K_s</i>	54,398	16.148	0.034
J1226	1	WISE	W1	55,370.140	14.304	0.013
J1226	1	WISE	W2	55,370.140	13.302	0.020
J1226	1	WISE	W3	55,370.743	10.519	0.073
J1226	1	WISE	W4	55,370.743	8.221	0.565

Table B1
(Continued)

Name	Epoch	Survey/Telescope	Band	MJD	Mag.	Uncertainty
J1226	2	ZTF	<i>g</i>	58,607.299	20.751	0.061
J1226	2	ZTF	<i>r</i>	58,583.255	20.674	0.052
J1226	2	ZTF	<i>i</i>	58,261.189	19.846	0.097
J1226	2	WISE	W1	58,638.071	15.005	0.024
J1226	2	WISE	W2	58,638.071	14.315	0.058
J1338	1	SDSS	<i>u</i>	52,053	19.884	0.041
J1338	1	SDSS	<i>g</i>	52,053	19.437	0.025
J1338	1	SDSS	<i>r</i>	52,053	19.032	0.020
J1338	1	SDSS	<i>i</i>	52,053	18.734	0.018
J1338	1	SDSS	<i>z</i>	52,053	18.433	0.036
J1338	1	UKIDSS	<i>Y</i>	54,989	17.700	0.026
J1338	1	UKIDSS	<i>J</i>	54,989	17.154	0.029
J1338	1	UKIDSS	<i>H</i>	54,989	16.437	0.017
J1338	1	UKIDSS	<i>K_s</i>	54,989	15.515	0.014
J1338	1	WISE	W1	55,211.722	13.818	0.010
J1338	1	WISE	W2	55,211.722	13.170	0.020
J1338	1	WISE	W3	55,315.574	10.741	0.069
J1338	1	WISE	W4	55,387.109	7.400	0.354
J1338	2	FLWO	<i>g</i>	57,887.197	19.578	0.032
J1338	2	FLWO	<i>r</i>	57,887.201	19.008	0.026
J1338	2	WISE	W1	57,765.450	15.033	0.029
J1338	2	WISE	W2	57,765.450	14.244	0.060

Note. We use photometry in the optical, NIR, and MIR that is closest to the X-ray observation epochs. We use PSF (AB) magnitudes in the optical and 2'' diameter aperture (Vega) magnitudes in the NIR. The WISE data are in Vega magnitudes.

ORCID iDs

Qian Yang  <https://orcid.org/0000-0002-6893-3742>
 Paul J. Green  <https://orcid.org/0000-0002-8179-9445>
 Chelsea L. MacLeod  <https://orcid.org/0000-0003-3422-2202>
 Richard M. Plotkin  <https://orcid.org/0000-0002-7092-0326>
 Scott F. Anderson  <https://orcid.org/0000-0002-6404-9562>
 Allyson Bieryla  <https://orcid.org/0000-0001-6637-5401>
 Francesca Civano  <https://orcid.org/0000-0002-2115-1137>
 Michael Eracleous  <https://orcid.org/0000-0002-3719-940X>
 Matthew Graham  <https://orcid.org/0000-0002-3168-0139>
 John J. Ruan  <https://orcid.org/0000-0001-8665-5523>
 Jessie Runnoe  <https://orcid.org/0000-0001-8557-2822>
 Xiurui Zhao  <https://orcid.org/0000-0002-7791-3671>

References

Abazajian, K. N., Adelman-McCarthy, J. K., Agüeros, M. A., et al. 2009, *ApJS*, **182**, 543
 Ai, Y., Dou, L., Yang, C., et al. 2020, *ApJL*, **890**, L29
 Almeida, A., Anderson, S. F., Argudo-Fernández, M., et al. 2023, arXiv:2301.07688
 Antonucci, R. 1993, *ARA&A*, **31**, 473
 Arnaud, K. A. 1996, in ASP Conf. Ser. 101, *Astronomical Data Analysis Software and Systems V*, ed. G. H. Jacoby & J. Barnes (San Francisco, CA: ASP), 17
 Ballo, L., Giustini, M., Schartel, N., et al. 2008, *A&A*, **483**, 137
 Barth, A. J., Voevodkin, A., Carson, D. J., & Woźniak, P. 2014, *AJ*, **147**, 12
 Becker, R. H., White, R. L., & Helfand, D. J. 1995, *ApJ*, **450**, 559
 Bellm, E. C., Kulkarni, S. R., Graham, M. J., et al. 2019, *PASP*, **131**, 018002
 Bennert, N., Falcke, H., Schulz, H., Wilson, A. S., & Wills, B. J. 2002, *ApJL*, **574**, L105
 Bianchi, S., Guainazzi, M., Matt, G., et al. 2005, *A&A*, **442**, 185
 Blanchard, P. K., Nicholl, M., Berger, E., et al. 2017, *ApJ*, **843**, 106
 Blandford, R. D., & Begelman, M. C. 1999, *MNRAS Lett.*, **303**, L1

Boroson, T. A., & Green, R. F. 1992, *ApJS*, **80**, 109
 Brightman, M., Silverman, J. D., Mainieri, V., et al. 2013, *MNRAS*, **433**, 2485
 Bruzual, G., & Charlot, S. 2003, *MNRAS*, **344**, 1000
 Cadolle Bel, M., Ribó, M., Rodríguez, J., et al. 2007, *ApJ*, **659**, 549
 Cardelli, J. A., Clayton, G. C., & Mathis, J. S. 1989, *ApJ*, **345**, 245
 CASA Team, Bean, B., Bhatnagar, S., et al. 2022, *PASP*, **134**, 114501
 Cash, W. 1979, *ApJ*, **228**, 939
 Chabrier, G. 2003, *PASP*, **115**, 763
 Chambers, K. C., Magnier, E. A., Metcalfe, N., et al. 2016, arXiv:1612.05560
 Chonis, T. S., Hill, G. J., Lee, H., et al. 2016, *Proc. SPIE*, **9908**, 99084C
 Corbel, S., Coriat, M., Brocksopp, C., et al. 2013, *MNRAS*, **428**, 2500
 Davidson, K., & Netzer, H. 1979, *RvMP*, **51**, 715
 Dawson, K. S., Schlegel, D. J., Ahn, C. P., et al. 2013, *AJ*, **145**, 10
 Debnath, D., Chakrabarti, S. K., & Nandi, A. 2010, *A&A*, **520**, A98
 Denney, K. D., De Rosa, G., Croxall, K., et al. 2014, *ApJ*, **796**, 134
 Dexter, J., & Begelman, M. C. 2019, *MNRAS Lett.*, **483**, L17
 Dey, A., Schlegel, D. J., Lang, D., et al. 2019, *AJ*, **157**, 168
 Dong, A.-J., Wu, Q., & Cao, X.-F. 2014, *ApJL*, **787**, L20
 Drake, A. J., Djorgovski, S. G., Mahabal, A., et al. 2009, *ApJ*, **696**, 870
 Dye, S., Lawrence, A., Read, M. A., et al. 2018, *MNRAS*, **473**, 5113
 Eisenstein, D. J., Weinberg, D. H., Agol, E., et al. 2011, *AJ*, **142**, 72
 Elitzur, M., Ho, L. C., & Trump, J. R. 2014, *MNRAS*, **438**, 3340
 Elvis, M., Wilkes, B. J., McDowell, J. C., et al. 1994, *ApJS*, **95**, 1
 Eracleous, M., Hwang, J. A., & Flohic, H. M. L. G. 2010, *ApJS*, **187**, 135
 Eracleous, M., Livio, M., Halpern, J. P., & Storchi-Bergmann, T. 1995, *ApJ*, **438**, 610
 Evans, I. N., Primini, F. A., Miller, J. B., et al. 2020, AAS Meeting, **235**, 154.05
 Fabian, A. C. 2012, *ARA&A*, **50**, 455
 Falcke, H., Körding, E., & Markoff, S. 2004, *A&A*, **414**, 895
 Fitzpatrick, E. L. 1999, *PASP*, **111**, 63
 Frederick, S., Gezari, S., Graham, M. J., et al. 2019, *ApJ*, **883**, 31
 Fruscione, A., McDowell, J. C., Allen, G. E., et al. 2006, *Proc. SPIE*, **6270**, 62701V
 Gabriel, C., Denby, M., Fyfe, D. J., et al. 2004, in ASP Conf. Ser. 314, *Astronomical Data Analysis Software and Systems (ADASS) XIII*, ed. F. Ochsenbein, M. G. Allen, & D. Egret (San Francisco, CA: ASP), 759
 Garmire, G. P., Bautz, M. W., Ford, P. G., Nousek, J. A., & Ricker, G. R. J. 2003, *Proc. SPIE*, **4851**, 28
 Gaskell, C. M., & Peterson, B. M. 1987, *ApJS*, **65**, 1

- Gezari, S., Hung, T., Cenko, S. B., et al. 2017, *ApJ*, **835**, 144
- Green, P. J., Pulgarin-Duque, L., Anderson, S. F., et al. 2022, *ApJ*, **933**, 180
- Gültekin, K., King, A. L., Cackett, E. M., et al. 2019, *ApJ*, **871**, 80
- Gunn, J. E., Siegmund, W. A., Mannery, E. J., et al. 2006, *AJ*, **131**, 2332
- Haardt, F., & Maraschi, L. 1993, *ApJ*, **413**, 507
- Heinz, S., & Sunyaev, R. A. 2003, *MNRAS*, **343**, L59
- Hickox, R. C., Mullaney, J. R., Alexander, D. M., et al. 2014, *ApJ*, **782**, 9
- Ho, L. C. 2008, *ARA&A*, **46**, 475
- Hon, W. J., Wolf, C., Onken, C. A., Webster, R., & Auchettl, K. 2022, *MNRAS*, **511**, 54
- Husemann, B., Urrutia, T., Tremblay, G. R., et al. 2016, *A&A*, **593**, L9
- Jin, X., Ruan, J. J., Haggard, D., et al. 2021, *ApJ*, **912**, 20
- Jonker, P. G., Miller-Jones, J., Homan, J., et al. 2010, *MNRAS*, **401**, 1255
- Just, D. W., Brandt, W. N., Shemmer, O., et al. 2007, *ApJ*, **665**, 1004
- Kalberla, P. M. W., Burton, W. B., Hartmann, D., et al. 2005, *A&A*, **440**, 775
- Kara, E., Steiner, J. F., Fabian, A. C., et al. 2019, *Natur*, **565**, 198
- Kaspi, S., Smith, P. S., Netzer, H., et al. 2000, *ApJ*, **533**, 631
- Kelly, B. C., Bechtold, J., & Siemiginowska, A. 2009, *ApJ*, **698**, 895
- Kishimoto, M., Hönig, S. F., Beckert, T., & Weigelt, G. 2007, *A&A*, **476**, 713
- Kormendy, J., & Ho, L. C. 2013, *ARA&A*, **51**, 511
- Koshida, S., Minezaki, T., Yoshii, Y., et al. 2014, *ApJ*, **788**, 159
- Koss, M., Trakhtenbrot, B., Ricci, C., et al. 2017, *ApJ*, **850**, 74
- Krolik, J. H. 1999, *Active Galactic Nuclei: from the Central Black Hole to the Galactic Environment* (Princeton, NJ: Princeton Univ. Press)
- LaMassa, S. M., Cales, S., Moran, E. C., et al. 2015, *ApJ*, **800**, 144
- LaMassa, S. M., Yaqoob, T., Ptak, A. F., et al. 2014, *ApJ*, **787**, 61
- Lang, D. 2014, *AJ*, **147**, 108
- Law, N. M., Kulkarni, S. R., Dekany, R. G., et al. 2009, *PASP*, **121**, 1395
- Lawrence, A., Warren, S. J., Almaini, O., et al. 2007, *MNRAS*, **379**, 1599
- López-Navas, E., Martínez-Aldama, M. L., Bernal, S., et al. 2022, *MNRAS Lett.*, **513**, L57
- Lusso, E., Comastri, A., Simmons, B. D., et al. 2012, *MNRAS*, **425**, 623
- Lusso, E., Comastri, A., Vignali, C., et al. 2010, *A&A*, **512**, A34
- Lyke, B. W., Higley, A. N., McLane, J. N., et al. 2020, *ApJS*, **250**, 8
- Lyu, B., Yan, Z., Yu, W., & Wu, Q. 2021, *MNRAS*, **506**, 4188
- Lyu, J., Rieke, G. H., & Smith, P. S. 2019, *ApJ*, **886**, 33
- Maccarone, T. J. 2003, *A&A*, **409**, 697
- MacLeod, C. L., Green, P. J., Anderson, S. F., et al. 2019, *ApJ*, **874**, 8
- MacLeod, C. L., Ivezić, Ž., Kochanek, C. S., et al. 2010, *ApJ*, **721**, 1014
- MacLeod, C. L., Ross, N. P., Lawrence, A., et al. 2016, *MNRAS*, **457**, 389
- Maiolino, R., Risaliti, G., Salvati, M., et al. 2010, *A&A*, **517**, A47
- Marchese, E., Braitto, V., Della Ceca, R., Caccianiga, A., & Severgnini, P. 2012, *MNRAS*, **421**, 1803
- Martini, P., & Schneider, D. P. 2003, *ApJL*, **597**, L109
- Matt, G., Guainazzi, M., & Maiolino, R. 2003, *MNRAS*, **342**, 422
- McElroy, R. E., Husemann, B., Croom, S. M., et al. 2016, *A&A*, **593**, L8
- McHardy, I. 2010, in *Lecture Notes in Physics*, ed. T. Belloni (Berlin: Springer), 203
- McMahon, R. G., Banerji, M., Gonzalez, E., et al. 2013, *Msngr*, **154**, 35
- Meisner, A. M., Caselden, D., Schlafly, E. F., & Kiwy, F. 2023, *AJ*, **165**, 36
- Merloni, A., Dwelly, T., Salvato, M., et al. 2015, *MNRAS*, **452**, 69
- Merloni, A., Heinz, S., & di Matteo, T. 2003, *MNRAS*, **345**, 1057
- Middei, R., Bianchi, S., Marinucci, A., et al. 2019, *A&A*, **630**, A131
- Munari, U., Sordo, R., Castelli, F., & Zwitter, T. 2005, *A&A*, **442**, 1127
- Narayan, R. 2005, *Ap&SS*, **300**, 177
- Narayan, R., & Yi, I. 1994, *ApJL*, **428**, L13
- Netzer, H. 2015, *ARA&A*, **53**, 365
- Noda, H., & Done, C. 2018, *MNRAS*, **480**, 3898
- Oh, K., Koss, M. J., Ueda, Y., et al. 2022, *ApJS*, **261**, 4
- Oppenheimer, B. D., Segers, M., Schaye, J., Richings, A. J., & Crain, R. A. 2018, *MNRAS*, **474**, 4740
- Pan, X., Li, S.-L., & Cao, X. 2021, *ApJ*, **910**, 97
- Panessa, F., Carrera, F. J., Bianchi, S., et al. 2009, *MNRAS*, **398**, 1951
- Páris, I., Petitjean, P., Aubourg, É., et al. 2018, *A&A*, **613**, A51
- Parker, M. L., Scharrel, N., Grupe, D., et al. 2019, *MNRAS Lett.*, **483**, L88
- Perley, R. A., Chandler, C. J., Butler, B. J., & Wrobel, J. M. 2011, *ApJL*, **739**, L1
- Peterson, B. M., Wanders, I., Horne, K., et al. 1998, *PASP*, **110**, 660
- Petrucci, P. O., Ursini, F., De Rosa, A., et al. 2018, *A&A*, **611**, A59
- Piconcelli, E., Fiore, F., Nicastro, F., et al. 2007, *A&A*, **473**, 85
- Pier, E. A., & Krolik, J. H. 1993, *ApJ*, **418**, 673
- Plotkin, R. M., Markoff, S., Kelly, B. C., Körding, E., & Anderson, S. F. 2012, *MNRAS*, **419**, 267
- Ricci, C., Bauer, F. E., Arevalo, P., et al. 2016, *ApJ*, **820**, 5
- Ricci, C., & Trakhtenbrot, B. 2022, arXiv:2211.05132
- Ricci, C., Trakhtenbrot, B., Koss, M. J., et al. 2017, *ApJS*, **233**, 17
- Ross, N. P., Graham, M. J., Calderone, G., et al. 2020, *MNRAS*, **498**, 2339
- Ruan, J. J., Anderson, S. F., Cales, S. L., et al. 2016, *ApJ*, **826**, 188
- Ruan, J. J., Anderson, S. F., Eracleous, M., et al. 2019, *ApJ*, **883**, 76
- Runnøe, J. C., Cales, S., Ruan, J. J., et al. 2016, *MNRAS*, **455**, 1691
- Salviander, S., Shields, G. A., Gebhardt, K., & Bonning, E. W. 2007, *ApJ*, **662**, 131
- Schawinski, K., Evans, D. A., Virani, S., et al. 2010, *ApJL*, **724**, L30
- Schlafly, E. F., & Finkbeiner, D. P. 2011, *ApJ*, **737**, 103
- Schlegel, D. J., Finkbeiner, D. P., & Davis, M. 1998, *ApJ*, **500**, 525
- Schneider, D. P., Richards, G. T., Hall, P. B., et al. 2010, *AJ*, **139**, 2360
- Schödel, R., Ott, T., Genzel, R., et al. 2002, *Natur*, **419**, 694
- Shakura, N. I., & Sunyaev, R. A. 1973, *A&A*, **24**, 337
- Shapovalova, A. I., Popović, L. Č, et al. 2019, *MNRAS*, **485**, 4790
- Shappee, B. J., Prieto, J. L., Grupe, D., et al. 2014, *ApJ*, **788**, 48
- Shen, Y., Hall, P. B., Horne, K., et al. 2019, *ApJS*, **241**, 34
- Sheng, Z., Wang, T., Jiang, N., et al. 2020, *ApJ*, **889**, 46
- Shields, G. A. 1978, *Natur*, **272**, 706
- Smee, S. A., Gunn, J. E., Uomoto, A., et al. 2013, *AJ*, **146**, 32
- Sniegowska, M., Czerny, B., Bon, E., & Bon, N. 2020, *A&A*, **641**, A167
- Sobolewska, M. A., Papadakis, I. E., Done, C., & Malzac, J. 2011, *MNRAS*, **417**, 280
- Stalewski, M., Fritz, J., Baes, M., Nakos, T., & Popović, L. Č. 2012, *MNRAS*, **420**, 2756
- Stalewski, M., Ricci, C., Ueda, Y., et al. 2016, *MNRAS*, **458**, 2288
- Stern, D., McKernan, B., Graham, M. J., et al. 2018, *ApJ*, **864**, 27
- Suganuma, M., Yoshii, Y., Kobayashi, Y., et al. 2006, *ApJ*, **639**, 46
- Tananbaum, H., Avni, Y., Branduardi, G., et al. 1979, *ApJL*, **234**, L9
- Thompson, A. R., Clark, B. G., Wade, C. M., & Napier, P. J. 1980, *ApJS*, **44**, 151
- Tody, D. 1986, *Proc. SPIE*, **627**, 733
- Tody, D. 1993, in *ASP Conf. Ser. 52, Astronomical Data Analysis Software and Systems II*, ed. R. J. Hanisch, R. J. V. Brissenden, & J. Barnes (San Francisco, CA: ASP), 173
- Trakhtenbrot, B., Arcavi, I., MacLeod, C. L., et al. 2019, *ApJ*, **883**, 94
- Traulsen, I., Schwöpe, A. D., Lamer, G., et al. 2020, *A&A*, **641**, A137
- Trichas, M., Green, P. J., Constantín, A., et al. 2013, *ApJ*, **778**, 188
- Tsuzuki, Y., Kawara, K., Yoshii, Y., et al. 2006, *ApJ*, **650**, 57
- Urry, C. M., & Padovani, P. 1995, *PASP*, **107**, 803
- Verolme, E. K., Cappellari, M., Copin, Y., et al. 2002, *MNRAS*, **335**, 517
- Vestergaard, M., & Peterson, B. M. 2006, *ApJ*, **641**, 689
- Vestergaard, M., & Wilkes, B. J. 2001, *ApJS*, **134**, 1
- Wang, J., Kara, E., Lucchini, M., et al. 2022, *ApJ*, **930**, 18
- Wright, E. L., Eisenhardt, P. R. M., Mainzer, A. K., et al. 2010, *AJ*, **140**, 1868
- Wu, Q., & Shen, Y. 2022, *ApJS*, **263**, 42
- Yang, G., Boquien, M., Buat, V., et al. 2020a, *MNRAS*, **491**, 740
- Yang, Q., Shen, Y., Chen, Y.-C., et al. 2020c, *MNRAS*, **493**, 5773
- Yang, Q., Shen, Y., Liu, X., et al. 2019, *ApJ*, **885**, 110
- Yang, Q., Shen, Y., Liu, X., et al. 2020b, *ApJ*, **900**, 58
- Yang, Q., Wu, X.-B., Fan, X., et al. 2018, *ApJ*, **862**, 109
- Zeltynt, G., Trakhtenbrot, B., Eracleous, M., et al. 2022, *ApJL*, **939**, L16
- Zu, Y., Kochanek, C. S., & Peterson, B. M. 2011, *ApJ*, **735**, 80